Boundary-value problem formulations for computing invariant manifolds and connecting orbits in the circular restricted three body problem

**R. C. Calleja · E. J. Doedel · A. R. Humphries ·
A. Lemus-Rodríguez · E. B. Oldeman**

Abstract We demonstrate the remarkable effectiveness of boundary value formulations coupled to numerical continuation for the computation of stable and unstable manifolds in systems of ordinary differential equations. Specifically, we consider the circular restricted three-body problem (CR3BP), which models the motion of a satellite in an Earth–Moon-like system. The CR3BP has many well-known families of periodic orbits, such as the planar Lyapunov orbits and the non-planar vertical and halo orbits. We compute the unstable manifolds of selected vertical and halo orbits, which in several cases leads to the detection of heteroclinic connections from such a periodic orbit to invariant tori. Subsequent continuation of these connecting orbits with a suitable end point condition and allowing the energy level to vary leads to the further detection of apparent homoclinic connections from the base periodic orbit to itself, or the detection of heteroclinic connections from the base periodic orbit to other periodic orbits. Some of these connecting orbits are of potential interest in space mission design.

R. C. Calleja · A. R. Humphries
Mathematics and Statistics, McGill University, 805 Sherbrooke O., Montreal,
QC H3A OB9, Canada
e-mail: calleja@math.mcgill.ca

A. R. Humphries
e-mail: tony.humphries@mcgill.ca

E. J. Doedel · E. B. Oldeman (✉)
Computer Science, Concordia University, 1455 Boulevard de Maisonneuve O., Montreal,
QC H3G 1M8, Canada
e-mail: boldeman@encs.concordia.ca

E. J. Doedel
e-mail: doedel@cse.concordia.ca

A. Lemus-Rodríguez
Mathematics and Statistics, Concordia University, 1455 Boulevard de Maisonneuve O., Montreal,
QC H3G 1M8, Canada
e-mail: a_lemusr@live.concordia.ca

1 Introduction

Numerical continuation of solutions to boundary value problems (BVPs) has been used exten-
sively to study periodic orbits and their bifurcations, including homoclinic and heteroclinic
orbits, in a wide variety of systems. For a recent overview see the articles in Krauskopf et al.
(2007). In particular, these techniques have been applied to compute families of periodic
orbits in the Circular Restricted 3-Body Problem (CR3BP); see, for example, Doedel et al.
(2003). In recent years invariant manifolds such as those in the Lorenz system have also been
computed in detail using numerical continuation (Krauskopf and Osinga 2007; Aguirre et al.
2011; Doedel et al. 2011). At the same time, continuation methods have been developed for
computing and continuing homoclinic and heteroclinic connecting orbits between periodic
orbits and equilibria or periodic orbits (Doedel et al. 2008, 2009; Krauskopf and Rieß 2008).
In the current work we use a combination of these techniques to illustrate their effectiveness
in computing stable and unstable manifolds and connecting orbits in the CR3BP.

There is much literature on invariant manifolds and connecting orbits in the CR3BP; see
for example Gómez et al. (2004), Koon et al. (2008), Lo and Ross (1997), Davis et al. (2010,
2011), Tantardini et al. (2010), Delshams et al. (2008). In particular, connecting orbits in the
planar CR3BP are well understood. The existence of connecting orbits in the planar problem
has been proved analytically in Llibre et al. (1985), and by computer assisted methods in
Wilczak and Zgliczyński (2003, 2005). Furthermore, these orbits have been extensively stud-
ied numerically using initial-value techniques and semi-analytical tools; see Barrabés et al.
(2009), Canalias and Masdemont (2006) and references therein. In the case of initial-value
techniques the initial conditions are varied in order for an appropriately chosen end point
condition to be satisfied. This approach is commonly referred to as a "shooting method" and,
for a more stable version, "multiple shooting". Initial-value techniques can also be very effec-
tive in the computation of invariant manifolds in the CR3BP. However, sensitive dependence
on initial conditions may leave parts of the manifolds unexplored, unless very high accuracy
is used. Other efficient methods for computing invariant manifolds include semi-analytical
approximations (Jorba and Masdemont 1999; Alessi et al. 2009; Gómez and Mondelo 2001).
The latter methods are very precise in a neighborhood of the center of expansion, and rely
on other methods to extend the manifolds outside these neighborhoods (Gómez et al. 2001).

Invariant manifold techniques around libration points have been used successfully in mis-
sion design (Lo et al. 2004). The Genesis spacecraft mission, designed to collect samples
of solar wind and return them to the Earth (Lo et al. 2001), is often considered as the first
mission to use invariant manifolds for its planning, while other missions have used libration
point techniques (Dunham and Farquhar 2003). Having a precise idea of the geometry of
invariant manifolds and their connections is desirable in the design of complex low thrust
missions.

Using our continuation approach we construct a continuous solution family in the man-
ifold as the initial value is allowed to vary along a given curve. The continuation step size
governs the distance between any computed trajectory and the next trajectory to be com-
puted. Here "distance" includes the change in the entire trajectory, and not only in the initial
conditions. In fact, this distance typically also includes other variables in the continuation
process, such as the integration time and the arclength of the trajectory. This formulation

allows the entire manifold to be covered, up to a prescribed length, integration time, or other termination criterion, even in very sensitive cases. Special orbits, such as connecting orbits to saddle-type objects, can be detected during the continuation. For example, a straightforward computation of the Lorenz manifold in this fashion yielded up to 512 connecting orbits having extremely close initial values, as reported in Doedel et al. (2006). In related work, the intersections of the Lorenz manifold with a sphere are studied in Aguirre et al. (2011) and Doedel et al. (2011). In the case of the Lorenz manifold, the sensitivity on initial conditions results from the significant difference in magnitude of the two real negative eigenvalues of the zero equilibrium that give rise to this manifold. Fixed precision integration in negative time may cover only part of this manifold, missing a portion in and near the direction of the eigenvector of the smaller negative eigenvalue.

In this paper we give an overview of continuation techniques, as used to compute periodic orbits, invariant manifolds, and connecting orbits. We also give several examples that illustrate how these techniques provide an effective and relatively easy-to-use tool for exploring selected portions of phase space. The richness of the solution structure of the CR3BP limits the extent of our illustrations. However, the techniques presented here are expected to be useful in further studies. In this respect, the current version of the freely available AUTO software (Doedel et al. 2010) includes demos that can be used to re-compute some of the numerical results presented here, including their graphical representation. These demos can also be adapted relatively easily to perform similar numerical studies of stable and unstable manifolds of other periodic orbits in the CR3BP that are not considered in this paper, as well as for entirely different applications.

This paper is organized as follows. In Sect. 2 we recall some well-known facts about the CR3BP, namely, its equilibria, the libration points, and the basic periodic solution families that will be considered in this paper, namely the planar Lyapunov orbits and the vertical, halo and axial families. In Sect. 3 we review how boundary value techniques are used to compute periodic orbits in conservative systems, and how these techniques can also be used to compute the eigenfunctions associated with selected Floquet multipliers. These data provide a linear approximation of the unstable manifold of the periodic orbit.

Section 4 describes the continuation method used for computing unstable manifolds of periodic orbits. This involves first setting up an extended system with both the periodic orbit and its eigenfunction. Using the resulting information an initial orbit within the manifold is computed. This orbit is then continued, as its starting point is free to vary along a line that is tangent to a linear approximation of the unstable manifold, thereby tracing out the manifold. The algorithm, using pseudo-arclength continuation, is not guaranteed to compute the whole manifold in a single computation, because obstacles may be encountered during the continuation. In such cases the manifold may be completed, for example, by additional continuations from different starting orbits, or by using a suitably adapted continuation procedure as is done in Doedel et al. (2011). However, the obstacles themselves are also of interest. They may correspond to orbits in the unstable manifold that require an arbitrary long time interval to reach a specified termination plane, because they pass arbitrarily close to a connecting orbit between the original unstable periodic orbit and another invariant object. In this way connecting orbits can be detected, as was done to detect the 512 heteroclinic connections presented in Doedel et al. (2006).

In Sect. 5 we show the results of computations of unstable manifolds of vertical V_1 and halo H_1 orbits. When the manifolds are computed to a sufficient distance from the original periodic orbit, we find what appear to be heteroclinic connecting orbits from the original periodic orbit to an invariant torus. The tori found this way must have saddle-type instability,

since the connecting orbit approaches it, but ultimately also leaves the neighborhood of the torus. Such connecting orbits may be more difficult to find with initial value integration.

In Sect. 6 we describe a method for continuing the periodic-orbit-to-torus connections as solutions of an 18-dimensional ODE, when the energy is allowed to vary. These computations lead to the detection of other interesting connecting orbits. Section 7 discusses three representative examples. First we consider a family of connections from H_1 halo orbits. These connections loop once around the Earth before approaching an invariant torus, which is itself close to the H_1 orbit. We refer to such a torus as a quasi-H_1 torus. During the continuation, with changing energy of the originating H_1 halo orbit, we encounter a number of interesting connecting orbits. Specifically, we find a homoclinic orbit from an H_1 halo orbit to itself that loops once around the Earth, a heteroclinic connection from a northern H_1 halo orbit to its southern counterpart, a heteroclinic connection to a planar L_1 Lyapunov orbit, and a connection to a 5:1 resonant orbit on a torus near the corresponding southern halo orbit. We also find a connecting orbit from an H_1 halo orbit to a torus on which the orbit bounces back and forth between a northern axial A_1 orbit and its southern counterpart. Each of these special connecting orbits occurs for a specific energy of the originating H_1 halo orbit (and of course, by conservation of energy, the orbit it connects to has the same energy). Secondly we study a family of connecting orbits from an H_1 halo orbit that loop four times around the Earth. We find connections to an L_2 Lyapunov orbit, an H_2 halo orbit, and to a 5:1 and a 6:1 resonant torus near the libration point $\mathscr{L}_2$. Thirdly, we consider a family of connecting orbits on the Moon-side of the unstable manifold of the H_1 halo orbits that connect directly (without looping around the Earth) to a torus near $\mathscr{L}_2$. We find an example of a direct connecting orbit from an H_1 halo orbit to a planar L_2 Lyapunov orbit. To the best of our knowledge, these connecting orbits have not been found before. We must stress, however, that from a space mission design point of view, these orbits are sensitive to initial conditions and would require control techniques to stay on them.

In Sect. 8, we discuss global theoretical aspects of our results and their relation to the existing literature. In particular we see that the connecting orbits from H_1 halo orbits to A_1 axial orbits or to L_1 or L_2 planar Lyapunov orbits are codimension-one in the dynamical systems sense, and hence should occur for specific values of the energy of the originating H_1 halo orbit, as we observed numerically. In contrast, homoclinic and heteroclinic connecting orbits between H_1 halo orbits, which were observed numerically, are codimension-two, and so should not normally occur. We show that the connecting orbits from the H_1 halo orbits to quasi-H_1 tori are generic, and suggest that the numerically observed homoclinic and heteroclinic connecting orbits between H_1 halo orbits are actually connections to quasi-H_1 tori where the minor radius of the torus is so small as to make the torus visibly (and for the purpose of space mission design) indistinguishable from the H_1 halo orbit that it envelopes.

Finally in Sect. 9 we discuss some computational aspects of our numerical computations, such as the discretization used, and typical computer time needed.

2 The circular restricted 3-body problem

The CR3BP describes the motion of a satellite S with negligible mass in three-dimensional physical space. The motion is governed by the gravitational attraction of two heavy bodies, which are assumed to rotate in circles around their common center of mass; see Fig. 1a. In this paper we call the heaviest body the "Earth" E, and the other heavy body the "Moon" M, and we use their actual mass ratio, namely, $\mu \approx 0.01215$. Any other mass ratio is allowed, such as for the Sun–Jupiter system, with a mass ratio of $\mu \approx 0.0009537$. Without loss of
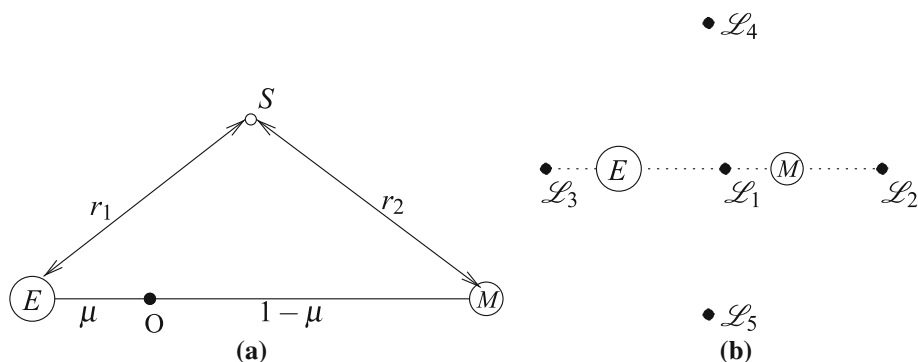
Fig. 1 **a** Schematic representation of the circular restricted three-body problem. **b** The five libration points

generality the total mass can be scaled to 1, so that the Earth and Moon have mass 0.98785 and 0.01215, respectively.

The equations of motion of the CR3BP as given in Danby (1992) are

$$
\begin{aligned}
\ddot{x} &= 2\dot{y} + x - (1 - \mu)\,\frac{x + \mu}{r_1{}^3} - \mu\,\frac{x - 1 + \mu}{r_2{}^3}, \\
\ddot{y} &= -2\dot{x} + y - (1 - \mu)\frac{y}{r_1{}^3} - \mu\,\frac{y}{r_2{}^3}, \\
\ddot{z} &= -(1 - \mu)\frac{z}{r_1{}^3} - \mu\,\frac{z}{r_2{}^3},
\end{aligned}
\tag{1}
$$

where (x, y, z) is the position of the zero-mass body, and where

$$
r_1 = \sqrt{(x + \mu)^2 + y^2 + z^2}, \quad r_2 = \sqrt{(x - 1 + \mu)^2 + y^2 + z^2},
$$

denote the distance from S to the Earth and to the Moon, respectively. The CR3BP has one integral of motion, namely, the energy E:

$$
\begin{aligned}
E &= \frac{\dot{x}^2 + \dot{y}^2 + \dot{z}^2}{2} + U(x, y, z), \\
U(x, y, z) &= -\frac{1}{2}(x^2 + y^2) - \frac{1 - \mu}{r_1} - \frac{\mu}{r_2} - \mu\frac{1 - \mu}{2},
\end{aligned}
$$

where $U(x, y, z)$ is the effective potential. Astronomers also often use the *Jacobi constant* C, defined as $C = -2E$.

Libration points, in both the planar and three-dimensional spatial system, are equilibrium points in a co-rotating frame; see Fig. 1b. As already used, we denote the libration points by $\mathscr{L}_1, \mathscr{L}_2, \ldots, \mathscr{L}_5$. There are families of periodic orbits (in the co-rotating frame) that bifurcate from each of these libration points, and we refer to these as the *primary families*. Many more families subsequently bifurcate from the primary families. We refer to the bifurcation points as *branch points*. Several families of periodic solutions of the Earth–Moon system are represented in Fig. 2; see also Doedel et al. (2003, 2007) and references therein. In the present work we focus on four families, namely, the vertical orbits V_i, the planar Lyapunov orbits L_i, the halo orbits H_i, and the axial orbits A_i. The families of planar Lyapunov orbits L_i and the vertical orbits V_i emanate directly from the libration points $\mathscr{L}_i$; these are primary families (Fig. 3). The families of halo orbits bifurcate from the families of Lyapunov orbits L_i, while the families of axial orbits connect and bifurcate from the V_i and L_i families.
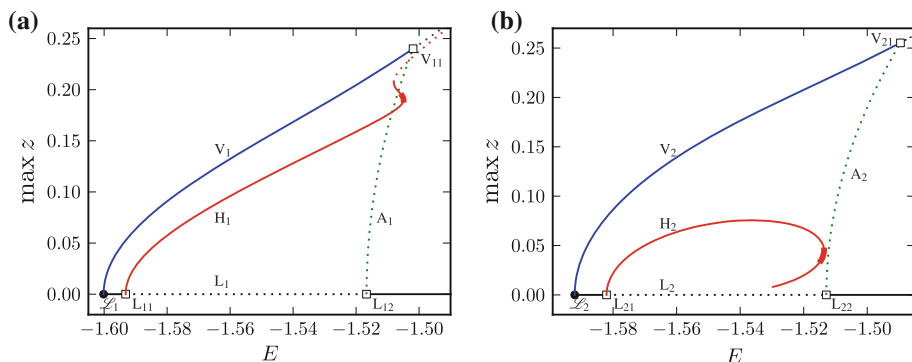
Fig. 2 Bifurcation diagrams of families of periodic solutions of the Earth–Moon system bifurcating from the libration points **a** $\mathscr{L}_1$ and **b** $\mathscr{L}_2$. A detailed description of the families represented in this diagram can be found in Doedel et al. (2007). The "*thick*" portions of the curves labeled H_1 and H_2 denote periodic orbits where all 6 Floquet multipliers are on the unit *circle*: 1, 1, $\exp(\pm ic)$, $\exp(\pm id)$. For *thin solid portions* exactly two real Floquet multipliers are off the unit circle: 1, 1, a, $1/a$, $\exp(\pm ic)$. The *dotted portions* denote periodic orbits where all 6 Floquet multipliers are real: 1, 1, a, $1/a$, b, $1/b$. Here $a, b, c, d \in \mathbb{R}$, $|a| > 1$, $|b| > 1$, and $c, d \in (0, \pi)$. The *small squares* labeled L_{ij} and V_{i1} denote branch points
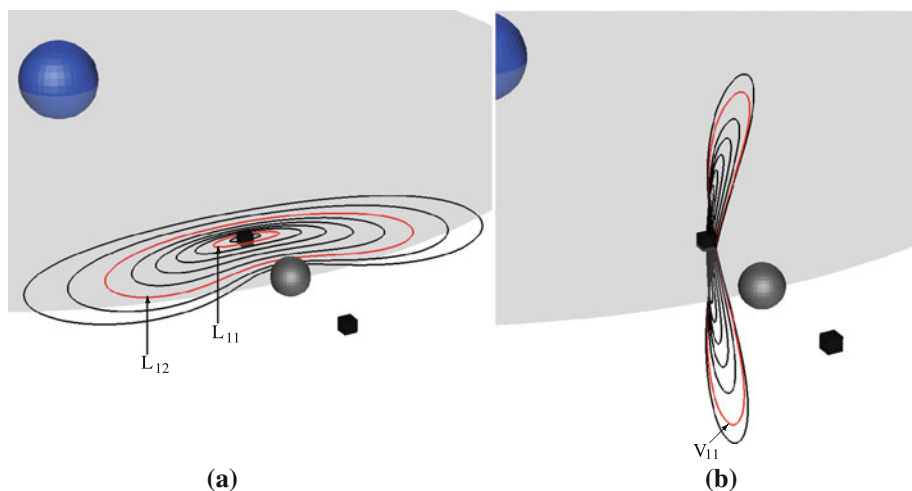

Fig. 3 **a** A selection of periodic orbits from the planar Lyapunov family L_1, which bifurcates from the libration point $\mathscr{L}_1$, as seen in the bifurcation diagram in Fig. 2a. Labeled are the special Lyapunov orbits L_{11} from which the halo family H_1 emanates, and L_{12} from which the axial family A_1 bifurcates. In this and subsequent figures the small cubes denote libration points. **b** Selected orbits from the vertical family V_1, which also bifurcates from the libration point $\mathscr{L}_1$. In the linear approximation near $\mathscr{L}_1$ these orbits are indeed "*vertical*", i.e., x and y are constant along it, with $y = 0$, while z oscillates around zero. The axial family bifurcates from the orbit labeled V_{11}

We refer to the halo and axial orbits as *secondary families* (Fig. 4). These families are all well-documented in the literature, but their names are sometimes different. For example, the halo, axial, and vertical orbits are known as type "A", "B", and "C", respectively, in Goudas (1961) and Hénon (1973). Farquhar (1968) coined the name "halo" for that family. The term "axial" comes from Doedel et al. (2007), whereas Doedel et al. (2003) used the term "Y" for "yellow".
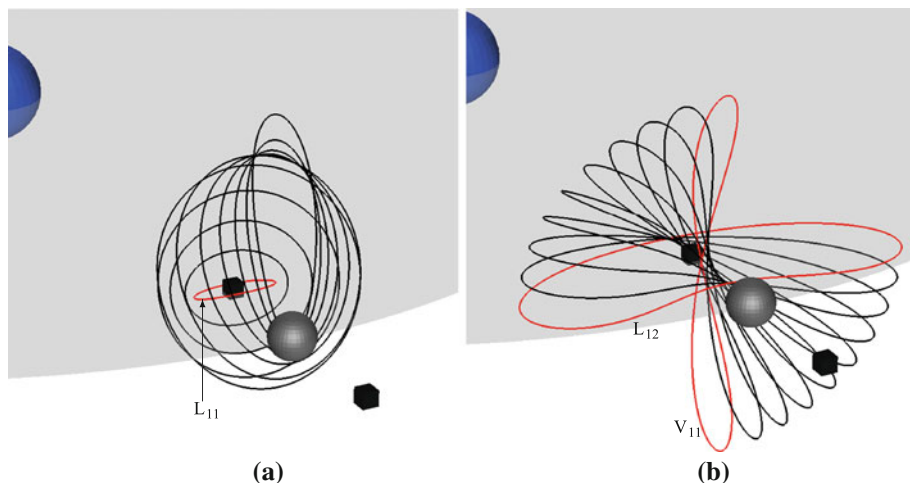
Fig. 4 **a** Selected orbits from the halo family H_1 that bifurcates from the Lyapunov family L_1 at L_{11}. **b** Selected orbits from the axial family A_1 that connects to the Lyapunov family L_1 at L_{12} and to the vertical family V_1 at V_{11}: see also Fig. 2

3 BVPs for periodic orbits and eigenfunctions

In this and the next section, we describe the algorithms used in the various stages of the computations in some detail, so that it will be possible for the reader to replicate the algorithms in other applications, and to better understand the functioning of the downloadable CR3BP demos (Doedel et al. 2010). Specifically, in this section we explain the preliminary computations that precede the actual computation of stable and unstable manifolds of periodic orbits, namely, the computation of the periodic orbits themselves and of their associated eigenfunctions. The discussion follows that in Doedel et al. (2003, 2008).

To formulate a suitable boundary value problem in AUTO, the second order system of ODEs (1) first needs to be rewritten as a six-dimensional first order system,

$$\dot{\mathbf{u}}(t) \ = \ \hat{\mathbf{f}}(\mathbf{u}(t), \mu), \qquad \hat{\mathbf{f}} : \mathbb{R}^6 \times \mathbb{R} \to \mathbb{R}^6,$$

where $\mathbf{u} = (x, y, z, v_x, v_y, v_z) = (x, y, z, \dot{x}, \dot{y}, \dot{z})$. As usual, when we plot the orbits graphically we project into $\mathbb{R}^3$ by only plotting the spatial coordinates (x, y, z). Time is scaled to the interval $[0, 1]$ in the BVP formulation for computing a periodic orbit, which changes the system of differential equations to

$$\dot{\mathbf{u}}(t) \ = \ T \, \hat{\mathbf{f}}(\mathbf{u}(t), \mu),$$

where T is the period of the periodic orbit. In addition, for a conservative system with one conserved quantity, we need to add a term with an "unfolding parameter" in order for the BVP continuation computations to be formally well-posed (Doedel et al. 2007; Muñoz-Almaraz et al. 2003); see also Muñoz-Almaraz et al. (2007). A suitable and convenient choice in the specific case of the CR3BP is the term $\sigma \mathbf{d}(\mathbf{u})$, where $\mathbf{d}(\mathbf{u}) = (0, 0, 0, v_x, v_y, v_z)$. The vector field with the unfolding term then becomes

$$\dot{\mathbf{u}}(t) \ = \ T \, \hat{\mathbf{f}}(\mathbf{u}(t), \mu) \ + \ \sigma \mathbf{d}(\mathbf{u}(t)),$$

which from here on we simply write as

$$\dot{\mathbf{u}}(t) \; = \; T \, \mathbf{f}(\mathbf{u}(t), \sigma), \tag{2}$$

also omitting the mass-ratio parameter μ, as it is typically fixed in the computation of families of periodic orbits. Notice that the specific choice of unfolding term $\mathbf{d}(\mathbf{u})$ used here would represent a damping (or forcing) term if $\sigma \neq 0$, which would preclude the existence of periodic orbits. However, the unfolding parameter σ is one of the unknowns in the continuation procedure, and will always be zero (to numerical precision) once solved for. Thus the unfolding term is simply a technical device necessary to obtain well-posedness of the BVP, and we do not force or damp the equations of motion.

Written in full, the system is therefore given by

$$\begin{aligned}
\dot{x} &= T \, v_x, \\
\dot{y} &= T \, v_y, \\
\dot{z} &= T \, v_z, \\
\dot{v}_x &= T \, [2v_y + x - (1-\mu)(x+\mu)r_1^{-3} - \mu(x-1+\mu)r_2^{-3}] + \sigma v_x, \\
\dot{v}_y &= T \, [-2v_x + y - (1-\mu)yr_1^{-3} - \mu y r_2^{-3}] + \sigma v_y, \\
\dot{v}_z &= T \, [-(1-\mu)zr_1^{-3} - \mu z r_2^{-3}] + \sigma v_z \, .
\end{aligned} \tag{3}$$

To complete the BVP formulation we need to add the periodicity equations

$$\mathbf{u}(1) \; = \; \mathbf{u}(0) \, . \tag{4}$$

If $\mathbf{u}(t)$ solves Eqs. (3) and (4) then $\mathbf{u}_\alpha(t) = \mathbf{u}(t+\alpha)$ is also a solution for any time-translation α. To specify a unique solution we impose the phase constraint (Doedel 1981)

$$\int_0^1 \langle \mathbf{u}(t), \dot{\mathbf{u}}_0(t) \rangle dt \; = \; 0, \tag{5}$$

where $\mathbf{u}_0(t)$ is the preceding computed solution along the solution family. Furthermore, for the purpose of continuing a family of periodic solutions, we add Keller's pseudo-arclength constraint (Keller 1977), which in the current setting takes the form

$$\int_0^1 \langle \mathbf{u}(t) - \mathbf{u}_0(t), \mathbf{u}_0'(t) \rangle dt + (T - T_0)T_0' + (\sigma - \sigma_0)\sigma_0' \; = \; \Delta s, \tag{6}$$

where $(\mathbf{u}_0, T_0, \sigma_0)$ corresponds to a computed solution along a solution family, $(\mathbf{u}, T, \sigma)$ is the next solution to be computed, and Δs is the continuation step size. The notation " $'$ " denotes the derivative with respect to Δs at $\Delta s = 0$ and $\langle \cdot, \cdot \rangle$ denotes the dot product. Since we are dealing with a conservative system, we already have families of periodic solutions even when the mass-ratio μ is fixed. For a computed solution $(\mathbf{u}_0, T_0, \sigma_0)$, and a given step Δs, the unknowns to be solved for in any continuation step are the periodic orbit $\mathbf{u}(t)$, its period T, and the unfolding parameter σ. Eq. 6 forces all of these unknowns to be close to those of the previous solution. In particular, $\mathbf{u}(t)$ must be close to $\mathbf{u}_0(t)$ for *all* t, and not just for $t = 0$. We reiterate that the unfolding parameter σ is an active unknown in the computations that regularizes the boundary value formulation, although it will be found to be zero to numerical precision. During the continuation the Floquet multipliers of the periodic solution are monitored by computing a special decomposition of the monodromy matrix that arises as a by-product of the decomposition of the Jacobian of the collocation system (Fairgrieve and Jepson 1991).

For the purpose of computing a stable or unstable manifold of a periodic orbit we need the corresponding Floquet eigenfunction. Specifically, we assume that the periodic orbit has a single, real, positive Floquet multiplier outside the unit circle in the complex plane, which gives rise to a two-dimensional unstable manifold of the periodic orbit in phase space. The eigenfunction corresponding to this multiplier provides a linear approximation to the manifold close to the periodic orbit. In Doedel et al. (2008) it is shown that this eigenfunction can be obtained as a solution $\mathbf{v}(t)$ of the BVP

$$\dot{\mathbf{v}}(t) = T\mathbf{f_u}(\mathbf{u}(t), 0)\mathbf{v}(t) + \lambda\mathbf{v}(t),$$
$$\mathbf{v}(1) = \pm\mathbf{v}(0), \tag{7}$$
$$\langle\mathbf{v}(0), \mathbf{v}(0)\rangle = \rho,$$

where $\mathbf{v}(1) = +\mathbf{v}(0)$ in the case of a positive multiplier, and $\mathbf{v}(1) = -\mathbf{v}(0)$ in the case of a negative multiplier. Here, λ is the characteristic exponent and the corresponding Floquet multiplier is given by $\pm e^{\lambda}$. Eq. (7) represents the Floquet eigenfunction/eigenvalue relation for the linearization of Eq. (2) about a periodic orbit $\mathbf{u}(t)$. The norm of the value of the eigenfunction at time $t = 0$ is normalized to be $\sqrt{\rho}$, where typically we use $\rho = 1$. If only one Floquet multiplier is real and greater than one in absolute value, this gives a unique (up to sign) unstable eigenfunction $\mathbf{v}(t)$. Likewise, a unique stable eigenfunction is obtained if only one Floquet multiplier is real and less than one in absolute value. In our illustrations we only compute unstable manifolds, so we have $\lambda > 0$ in Eq. (7); however all algorithms apply equally well to stable manifolds. We also restrict to the case where the Floquet multiplier of interest is positive, so $\mathbf{v}(1) = +\mathbf{v}(0)$ in Eq. (7), and the corresponding manifold is orientable rather than twisted. A linear approximation of the unstable manifold at time zero is then given by

$$\mathbf{r}(0) = \mathbf{u}(0) + \varepsilon\mathbf{v}(0), \tag{8}$$

for ε small.

An alternative formulation is to put the actual Floquet multiplier in the boundary condition rather than in the linearized differential equation, using the variational equation $\dot{\mathbf{v}}(t) = T\mathbf{f_u}(\mathbf{u}(t), 0)\mathbf{v}(t)$ and boundary condition $\mathbf{v}(1) = \kappa\mathbf{v}(0)$, where κ is the actual Floquet multiplier. However, the formulation in Eq. (7), as used here, has been found to be more appropriate for numerical purposes (Doedel et al. 2008). This is related to the fact that the multipliers, i.e., the values of $\kappa = e^{\lambda}$, can be very large or very small.

The algorithmic steps that lead to the linear approximation of the unstable manifold are then as follows; here described for the case of a halo orbit in the H_1 family.

1. The libration points, which are the equilibria of Eq. (1), are easily determined (Szebehely 1967). In our continuation context we note that they have zero velocity components, as well as $z = 0$, and that for varying μ their x and y components lie on connected curves, as shown in Fig. 5. Starting from, for example, the curve of equilibria $x^2 + y^2 = 1$, that exists when $\mu = 0$ (the curve containing the point q in Fig. 5), the libration points bifurcate from $x = 1/2, y = \pm\sqrt{3}/2$ and $y = 0, x = \pm 1$ and we can reach each of the libration points at any given nonzero value of μ via a connected path. The eigenvalues of the target libration point(s) are also computed.

2. Compute the target halo orbit in the H_1 family for which the unstable manifold is to be computed:
    The libration point $\mathscr{L}_1$ has two pairs of purely imaginary eigenvalues and a pair of real eigenvalues. The two pairs of purely imaginary eigenvalues correspond to the planar Lyapunov family L_1 and vertical family V_1 that bifurcate from $\mathscr{L}_1$. Compute the family

Fig. 5 Computation of the
libration points. The point q on
the circle of equilibria is a
suitable starting point for
determining the libration points
for a given nonzero value of μ by
continuation. For clarity, the five
libration points are indicated in
the diagram for the case
$\mu = 0.25$, rather than for the
Earth–Moon case ($\mu = 0.01215$),
as μ is close to zero in the latter
case. The *small squares* are
branch points
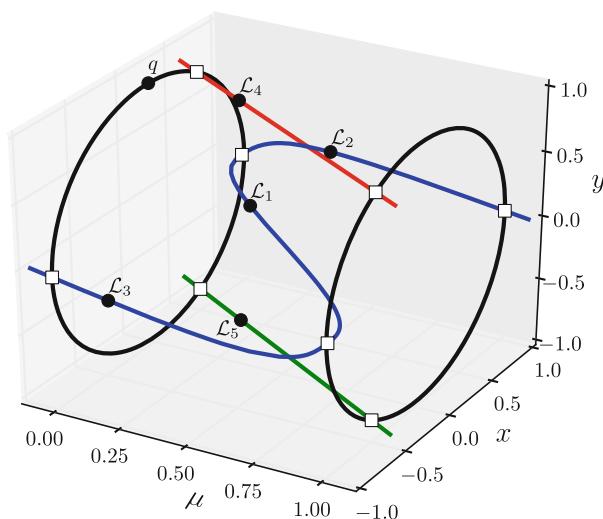
L$_1$, using a standard starting procedure (Doedel 1981) at the libration point $\mathcal{L}_1$. The free
problem parameters in this continuation are the period T and the unfolding parameter
σ. Along L$_1$ two branch points are located; see Fig. 3. Branch switching at the first of
these branch points gives the halo family H$_1$.

3. Determine the eigenfunction of a selected halo orbit:
   Select an appropriate periodic orbit in the H$_1$ family that has one real Floquet multiplier
   with absolute value greater than 1, so that its unstable manifold is two-dimensional.
   Compute the corresponding unstable eigenfunction as follows: couple the boundary
   value equations for $\mathbf{v}$ in Eq. (7) to those for $\mathbf{u}$ in Eqs. (2), (4), (5). Supplement this
   extended system by an appropriate continuation equation of the form of Eq. (6), that
   also includes $\mathbf{v}$, λ, and ρ, with $\mathbf{v}$ and ρ initialized to zero, and λ initialized to the desired
   Floquet exponent as obtained from the decomposition of the Jacobian of the collocation
   equations. Written out, this gives

$$
\begin{aligned}
&\dot{\mathbf{u}}(t) = T\mathbf{f}(\mathbf{u}(t), \sigma), \\
&\mathbf{u}(1) = \mathbf{u}(0), \\
&\int_0^1 \langle \mathbf{u}(t), \dot{\mathbf{u}}_0(t) \rangle dt \;=\; 0, \\
&\dot{\mathbf{v}}(t) = T\mathbf{f_u}(\mathbf{u}(t), 0)\mathbf{v}(t) + \lambda\mathbf{v}(t), \\
&\mathbf{v}(1) = \mathbf{v}(0), \\
&\langle \mathbf{v}(0), \mathbf{v}(0) \rangle = \rho, \\
&\int_0^1 \langle \mathbf{w}(t) - \mathbf{w}_0(t), \mathbf{w}_0'(t) \rangle dt + \langle \mathbf{p} - \mathbf{p}_0, \mathbf{p}_0' \rangle = \Delta s, \quad \mathbf{w}(t) = (\mathbf{u}(t), \mathbf{v}(t)), \; \mathbf{p} = (\sigma, \lambda, \rho).
\end{aligned}
\tag{9}
$$

In our continuation context we observe that the target period orbit $\mathbf{u}(t)$, together with
$\mathbf{v}(t) \equiv 0$ and $\mathbf{p} = (\sigma, \lambda, \rho) = (0, \lambda, 0)$), corresponds to a *branch point*, from which
a solution family $(\mathbf{u}, \mathbf{v}; \sigma, \lambda, \rho)$ bifurcates. Along this bifurcating family the orbit $\mathbf{u}(t)$
remains equal to the target periodic orbit, the Floquet exponent λ and the period T of

$\mathbf{u}(t)$ remain constant, while the unfolding parmameter σ remains zero; all to numerical precision. On the other hand, the Floquet eigenfunction $\mathbf{v}(t)$ becomes nonzero, and consequently ρ also becomes nonzero. In fact, one continuation step along the bifurcating family would be enough to obtain the nonzero eigenfunction $\mathbf{v}(t)$. However, for numerical purposes we typically do a few continuation steps along the bifurcating family until ρ is equal to 1, i.e., until the norm of the Floquet eigenfunction equals 1. This simple procedure to determine the Floquet eigenfunction fits well into the continuation and branch-switching algorithms in AUTO, it is numerically stable, and has the additional advantage that the Floquet eigenfunction, once computed, can be continued with fixed nonzero ρ and varying energy. In that case $\mathbf{p} = (\sigma, \lambda, T)$ in the last constraint of Eq. (9). This allows the determination of the eigenfunction $\mathbf{v}$ in highly sensitive cases, for example, for very large or very small Floquet multipliers.

Once the periodic orbit and its appropriate eigenfunction have been computed, we can proceed to compute the manifold.
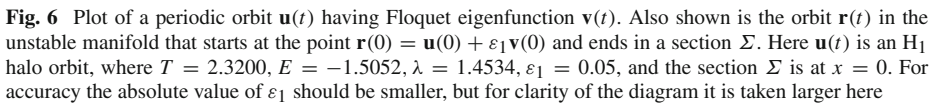
4 Basic computation of unstable manifolds

Here we describe a method for computing unstable manifolds based on the continuation of orbits that lie in it. These orbits start (as a function of time) in the linear approximation of the unstable manifold that was computed above, and end in a section where one of the coordinates is fixed. Other possibilities to constrain the end point include fixing the integration time or the arclength; we found the fixed end section to be the most appropriate here. All these approaches are robust against sensitive dependence on initial conditions; see also Krauskopf and Osinga (2007).

We now explain the procedure for computing the unstable manifolds of a given periodic orbit $\mathbf{u}(t)$ in some detail. We assume that $\mathbf{u}(t)$ has one real Floquet multiplier with absolute value greater than 1, with associated eigenfunction $\mathbf{v}(t)$, computed as described in Sect. 3. The starting data needed are a point on the periodic orbit, namely $\mathbf{u}(0)$, and the corresponding value of the Floquet eigenfunction, namely $\mathbf{v}(0)$. For a given appropriately small value of ε_1, take the point $\mathbf{r}(0) = \mathbf{u}(0) + \varepsilon_1 \mathbf{v}(0)$ as the starting point of an orbit $\mathbf{r}(t)$ in the unstable manifold; see Fig. 6. Here t denotes the time along the orbit $\mathbf{r}(t)$. Similar to the case of the periodic orbit $\mathbf{u}(t)$ and its eigenfunction $\mathbf{v}(t)$, where for numerical reasons the time interval was rescaled from $[0, T]$ to $[0, 1]$, for the non-periodic orbit $\mathbf{r}(t)$ we also rescale time to the unit interval. Select a section Σ, for example, at $x_\Sigma = 0$ or $x_\Sigma = -0.25$, where the orbit $\mathbf{r}(t)$ is to terminate; i.e., $\mathbf{r}(1) \in \Sigma$. (We may allow the orbit $\mathbf{r}(t)$ to cross Σ several times, before it actually terminates in Σ.) The part of the manifold to be approximated is then given by the set of orbits

$$\{\mathbf{r}(t) \mid \mathbf{r}(0) = \mathbf{u}(0) + \varepsilon \mathbf{v}(0) \text{ and } \mathbf{r}(1) \in \Sigma, \text{ for } \varepsilon_1 \leq \varepsilon < \varepsilon_2\}. \tag{10}$$

The range of values of ε, namely, $[\varepsilon_1, \varepsilon_2)$, should be chosen to correspond to a *fundamental domain*, see Fig 6. This ensures that the full manifold is swept out, at least locally near the periodic orbit, as ε is allowed to vary from ε_1 to ε_2. If the interval $[\varepsilon_1, \varepsilon_2]$ is chosen too small then the manifold would be incomplete. Taking this interval too large would lead to duplication of orbits, albeit having different lengths. A fundamental domain is such that the orbit that starts at $\mathbf{u}(0) + \varepsilon_1 \mathbf{v}(0)$ closely passes the line given by $\mathbf{u}(0) + \varepsilon \mathbf{v}(0)$ again, for the first time, at $\mathbf{u}(0) + \varepsilon_2 \mathbf{v}(0)$. For a given value of ε_1, using fundamental properties of

Fig. 6 Plot of a periodic orbit $\mathbf{u}(t)$ having Floquet eigenfunction $\mathbf{v}(t)$. Also shown is the orbit $\mathbf{r}(t)$ in the unstable manifold that starts at the point $\mathbf{r}(0) = \mathbf{u}(0) + \varepsilon_1 \mathbf{v}(0)$ and ends in a section Σ. Here $\mathbf{u}(t)$ is an H_1 halo orbit, where $T = 2.3200$, $E = -1.5052$, $\lambda = 1.4534$, $\varepsilon_1 = 0.05$, and the section Σ is at $x = 0$. For accuracy the absolute value of ε_1 should be smaller, but for clarity of the diagram it is taken larger here

the eigenfunction $\mathbf{v}(t)$ we can compute the corresponding linear approximation of ε_2 using $\varepsilon_2 = e^{\lambda} \varepsilon_1$.

We also note that if ε_1 is too small in absolute value then the orbit $\mathbf{r}(t)$ remains close to the periodic orbit for a long time before it escapes to ultimately reach the section Σ. If, on the other hand, ε_1 is too large in absolute value then the linear approximation of the manifold is no longer accurate.

The boundary value problem for $\mathbf{r}(t)$ is then given by

$$
\begin{aligned}
\dot{\mathbf{r}}(t) &= T_r \, \mathbf{f}(\mathbf{r}(t), 0), \\
\mathbf{r}(0) &= \mathbf{u}(0) + \varepsilon \mathbf{v}(0), \\
\mathbf{r}(1)_x &= x_{\Sigma}, \\
\int_0^1 \langle \mathbf{r}(t) - \mathbf{r}_0(t), \mathbf{r}_0'(t) \rangle dt &+ (\varepsilon - \varepsilon_0)\varepsilon_0' + (T_r - T_{r0})T_{r0}' = \Delta s,
\end{aligned}
\tag{11}
$$

where $\sigma = 0$ in $\mathbf{f}(\mathbf{r}(t), \sigma)$, and Σ denotes the section $x = x_{\Sigma}$. As done earlier for the periodic orbit and for its eigenfunction, the actual integration time T_r of the orbit $\mathbf{r}(t)$ appears explicitly in the differential equation, due to the above-mentioned scaling of the time t. The pseudo-arclength constraint, the last equation in Eq. (11) plays a crucial role in the algorithm. For a given step size Δs the pseudo-arclength constraint ensures in particular that the next computed orbit $\mathbf{r}(t)$ is close to $\mathbf{r}_0(t)$ over the whole trajectory, and that also T_r is close to T_{r0}. The step size Δs could in principle be constant, but for efficiency and robustness it is adjusted after each successful continuation step, depending on the speed of convergence of the Newton-chord iterations.

Given the point $\mathbf{u}(0)$ on the periodic orbit, and the point $\mathbf{r}(0) = \mathbf{u}(0) + \varepsilon_1 \mathbf{v}(0)$ in the direction of the unstable manifold at time $t = 0$, the complete procedure to compute the manifold is then as follows:

1. Compute a *starting orbit* in the manifold, using continuation to do the "time integration". More precisely, we use numerical continuation with T_r as free parameter to compute a "family" of solutions, i.e., the same trajectory, but for a set of increasing integration times T_r. The equations used are

$$\dot{\mathbf{r}}(t) = T_r \, \mathbf{f}(\mathbf{r}(t), 0),$$
$$\mathbf{r}(0) = \mathbf{u}(0) + \varepsilon_1 \mathbf{v}(0), \tag{12}$$

which correspond to Eq. (11), but without the end point constraint. Note that ε is fixed at $\varepsilon = \varepsilon_1$ in each continuation step of this starting procedure. The continuation is stopped when $\mathbf{r}(1)$ intersects the plane Σ. (This termination point need not necessarily be the first such intersection.) The starting orbit in this continuation is the constant solution $r(t) \equiv \mathbf{u}(0) + \varepsilon_1 \mathbf{v}(0)$, with $T_r = 0$. Although it may appear inefficient to do a time-integration by continuation, this approach has the advantage that it fits very well into the continuation framework of the algorithms in this paper.

2. Given an orbit that ends in Σ, as computed above, the unstable manifold is then approximated by further continuation of this orbit, now using the boundary value problem in Eq. (11), with the end point $\mathbf{r}(1)$ constrained to remain in Σ, and with ε and the integration time T_r allowed to vary. If ε varies along a full fundamental domain, the continuation would sweep out the full unstable manifold, limited only by the termination condition. However, the pseudo-arclength constraint in Eq. (11) limits the size of the change in the orbit *and* in the the parameters in any continuation step. Hence the full unstable manifold is only obtained if no "obstacles" are encountered, where for example T_r goes to infinity. As will be seen in the next section, these obstacles can in fact be of much interest.

5 Example computations of unstable manifolds and connecting orbits to invariant tori

In this section we illustrate the basic boundary value technique described above by computing unstable manifolds of the vertical family V_1 and the halo family H_1. For certain ranges of their energy (the thin solid curves in Fig. 2) and period these families have periodic orbits with one real, positive Floquet multiplier outside the unit circle, so that their unstable manifold is indeed two-dimensional. The algorithm applies in principle also to higher-dimensional unstable manifolds, by using a selected unstable Floquet multiplier, typically the largest one, and its associated eigenfunction. As already mentioned, the algorithm also applies to stable manifolds. However, here we restrict attention to examples with two-dimensional unstable manifolds.

Figure 7 shows the computed unstable manifold of an orbit from the vertical family V_1. Here the section Σ is taken at $x_\Sigma = 0$. As seen in the figure, the orbits in the manifold terminate in Σ at their second intersection with this plane. Note also that the intersection curve of the manifold with the section Σ has a similar shape as the figure-eight vertical orbit from which the manifold originates.

Figure 8 shows the computed unstable manifold of a halo orbit from the H_1 family. The plane Σ is located at $x_\Sigma = -0.25$. Note that the manifold changes shape as it propagates. Here, as well as for the unstable manifold of the V_1 orbit, there is no contradiction in the fact that the cross section of the manifold with the plane Σ is a self-intersecting curve, since we are viewing a projection of the manifold from $\mathbb{R}^6$ (spatial and velocity variables) into $\mathbb{R}^3$ (spatial variables only).

If the section is taken at certain other value-ranges of x_Σ then one may encounter obstacles that prevent the continuation to cover the full manifold. More specifically, the initial value of the orbits, as determined by the value of ε, does not cover the entire fundamental domain, but approaches a particular value where $T_r \to \infty$. One possible scenario is that the orbit picks up additional loops around a torus-like object near its end point, if such an object exists, before returning to and ending in the plane Σ. This computational phenomenon is not exceptional in the CR3BP; in fact it is easy to find specific examples. One such
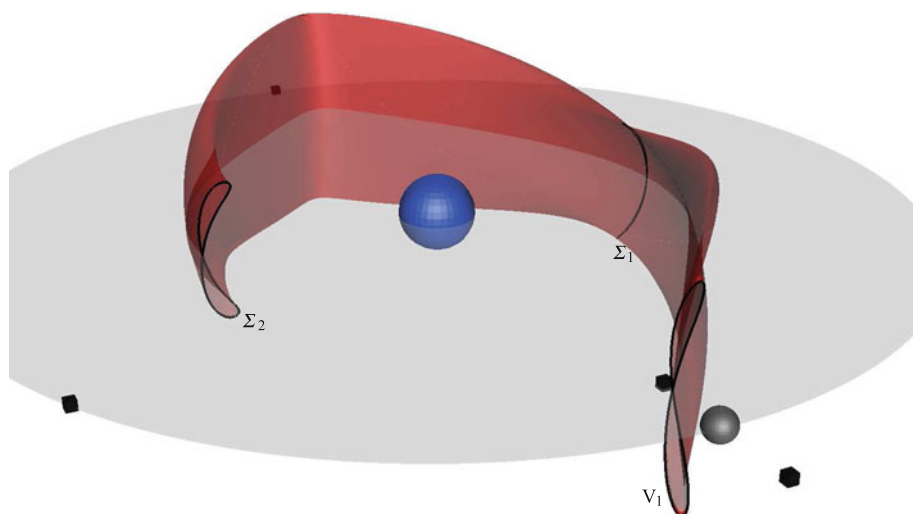
Fig. 7 The unstable manifold of a periodic orbit from the V_1 family. The periodic orbit, labeled V_1, is located on the $\mathcal{L}_1$ side of the Moon, with period $T = 3.7700$ and energy $E = -1.5164$. The terminating plane Σ is located at $x_\Sigma = 0$. The first intersection of the manifold with Σ is indicated by the curve labeled Σ_1, and the second intersection, where the manifold computation is terminated, is labeled Σ_2
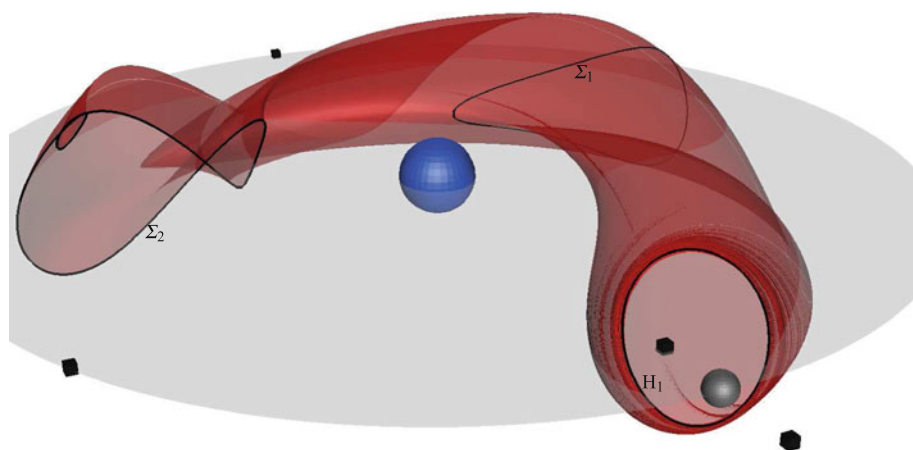

Fig. 8 The unstable manifold of a periodic orbit (labeled H_1) from the H_1 family. The periodic orbit, which is on the $\mathcal{L}_1$ side of the Moon, has period $T = 2.5152$ and energy $E = -1.5085$. The terminating plane Σ is located at $x_\Sigma = -0.25$, and the first and second intersections of the manifold with Σ are labeled Σ_1 and Σ_2

instance is given in Fig. 9, which again shows the unstable manifold of the vertical orbit in Fig. 7, but with a superimposed longer orbit that lies in the same unstable manifold. This longer orbit alone is shown separately in Fig. 10. As is evident from Fig. 10, the orbit returns to a neighborhood of the original vertical orbit, where it winds around a torus-like object (a *quasi-vertical* orbit).

More specifically, the phenomenon shown in Figs. 9 and 10 results from "growing" (see step 1 at the end of Sect. 4) a longer initial orbit in the unstable manifold of the V_1 periodic orbit, with ε fixed, until it intersects a plane Σ located at $x_\Sigma = 0.5$. Continuing this orbit
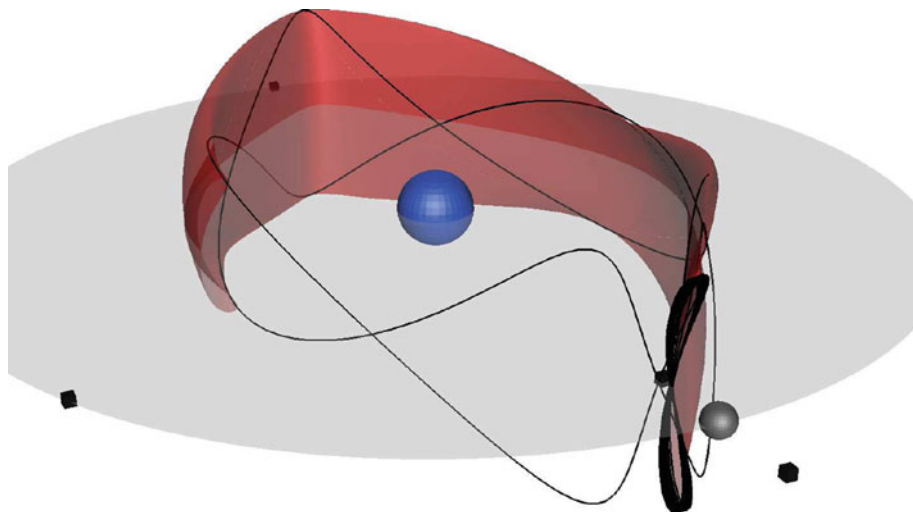
Fig. 9 Part of the unstable manifold of the V_1 periodic orbit from Fig. 7, together with a superimposed longer orbit in this manifold, computed as described in the text
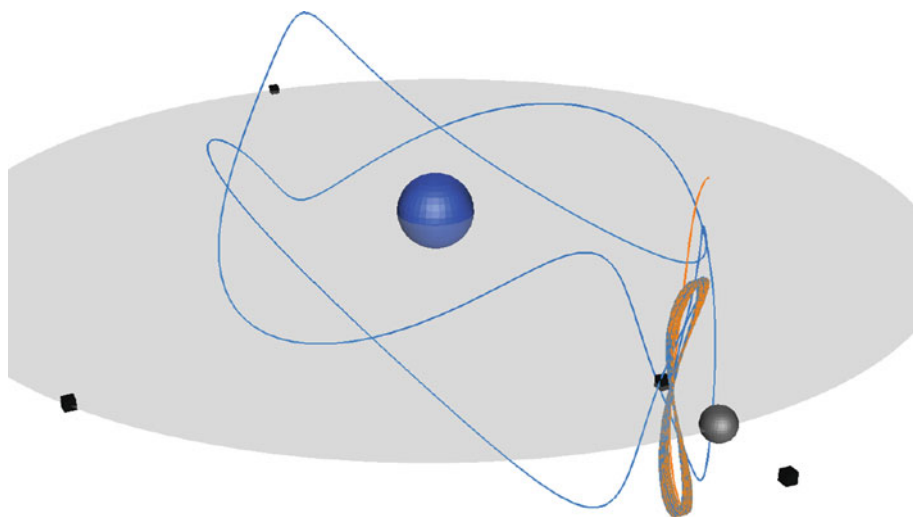

Fig. 10 A separate view of the longer orbit from Fig. 9, which winds around a torus near the original V_1 periodic orbit. The orbit ultimately returns to the plane Σ that is located at $x_\Sigma = 0.5$. We remark that in this and subsequent figures the orbit color changes from a deep *sky blue* [*RGB* code (0,0.5,1)] via *gray* [code (0.5,0.5,0.5)] to *dark orange* [code (1.0,0.5,0)] as the scaled time increases from 0 to 1

with the end point constrained to remain in Σ, and with ε and T_r allowed to vary, then results in it winding around a torus near the original V_1 periodic orbit, before returning to and terminating in the plane Σ. In contrast, trying to obtain such an orbit directly by shooting techniques appears to be difficult, as such orbits approach but then divert from the torus; see Fig. 11. Indeed, for the orbits to agree it may be necessary to compute the BVP orbits to higher precision, i.e., more than the double precision used in AUTO. In particular, this would yield the initial value to higher precision. Likewise, the initial value integration, starting from such a more accurate initial value, may also need to be in high precision arithmetic.
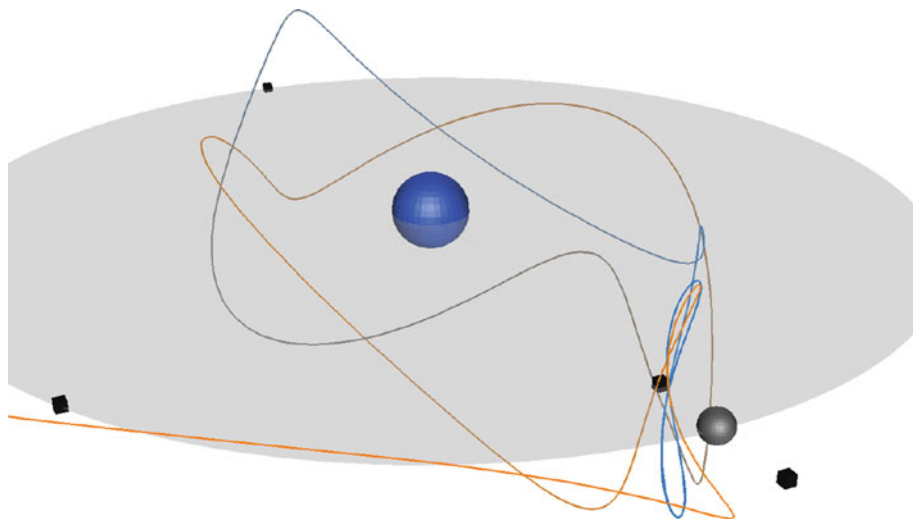
Fig. 11 An orbit obtained by initial value integration for the same value of ε, within numerical precision, as used for the orbit in Fig. 10. Note that the orbit approaches but then diverts from the torus seen in Fig. 10, without winding around it
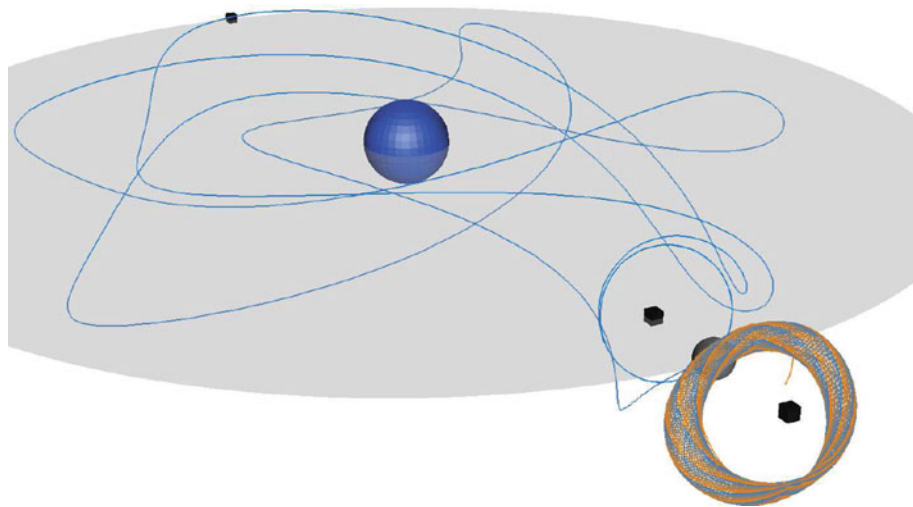

Fig. 12 Continuation of longer orbit within the unstable manifold of a halo orbit with $E = -1.5532$ with the plane Σ located at $x_\Sigma = 1.02$, that is, on the $\mathscr{L}_2$-side of the Moon. This orbit winds around a torus near an orbit from the halo family H_2, before returning to and ending in the plane Σ

A similar result is shown in Fig. 12 for an extended orbit from the H_1 manifold shown in Fig. 8. Here an orbit in the unstable manifold of the H_1 periodic orbit is grown until it reaches a plane Σ located at $x_\Sigma = 1.02$, i.e., on the $\mathscr{L}_2$-side of the Moon. Constraining the end point of this longer orbit to remain in Σ, and allowing ε to vary, then results in the end portion of the orbit to wind around a torus near an orbit from the halo family H_2 (a *quasi-halo* orbit), as shown in Fig. 12. Meanwhile the initial value $\mathbf{r}(0)$ of the orbit approaches a point in the fundamental domain, without fully covering that domain. Ultimately the orbit returns to the plane $x_\Sigma = 1.02$, as required by the computational set-up.

Similarly, in Fig. 13 an extended orbit from the H_1 manifold is grown until it reaches a plane Σ located at $x_\Sigma = 0.6$, after going around the Earth once. Constraining the end point of this orbit to Σ, while ε and the integration time T_r are allowed to vary, results in an orbit that winds around a quasi-halo orbit near H_1.

As a final example in this section we compute an initial orbit in the unstable manifold of an H_1 halo orbit, but now in the part of the unstable manifold on the side of the Moon. The terminating plane Σ was taken at $x_\Sigma = 1.02$. Further continuation of this orbit with x_Σ constrained to remain in Σ, and with ε allowed to vary, results in the end portion of this orbit winding around a quasi-halo orbit near an H_2 halo orbit, as shown in Fig. 14, before returning to and ending in Σ.

In this section we have computed the unstable manifolds of some orbits in the H_1 halo and V_1 vertical families. For certain values of ε we find what appear to be heteroclinic connecting orbits from the original periodic orbit to an invariant torus. These connecting orbits appear to be more difficult to obtain with shooting techniques. This was seen in Fig. 11, where shooting
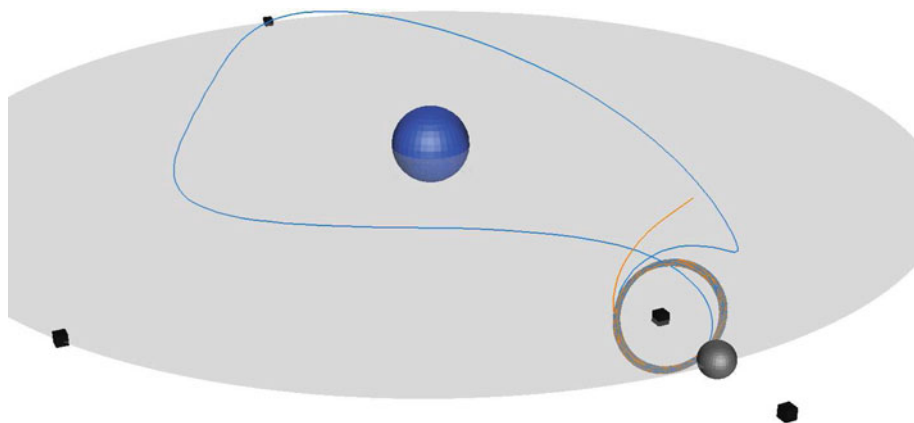

Fig. 13 Continuation of a longer orbit within the unstable manifold of a halo orbit with $E = -1.5631$ with the plane Σ located at $x_\Sigma = 0.6$. This orbit winds around a torus near the orbit from the halo family H_1 where it started from, before returning to and ending in the plane Σ
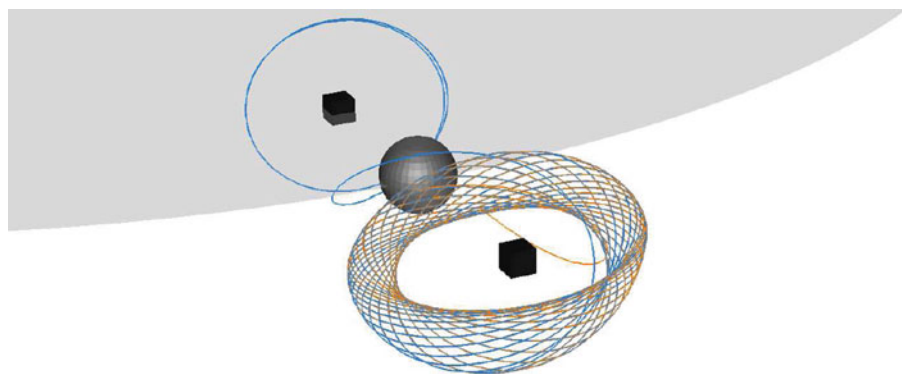

Fig. 14 An orbit in the Moon-side part of the unstable manifold of an H_1 periodic orbit. This orbit is found by fixing its end point to remain in a plane Σ located at $x_\Sigma = 1.02$, that is, on the $\mathscr{L}_2$-side of the Moon. The orbit winds around a torus near an orbit from the halo family H_2, before returning to and ending in the plane Σ

failed to reveal the invariant torus, when starting near the numerical value of ε for which the heteroclinic connection was found in the BVP approach. This is in part due to the fact that the tori are evidently unstable, with saddle-type stability since the connecting orbit approaches it, but ultimately also leaves the neighborhood of the torus.

The next objective is to continue the orbit-to-torus connections as the energy E is allowed to vary, and with it the base periodic orbit itself. In the following section we explain the computational set-up, while examples are given in Sect. 7. In particular we will see in Sect. 7 how such continuation can lead to homoclinic and heteroclinic connecting orbits between periodic orbits in the same or different families.

6 Continuation of connecting orbits

The examples in the preceding section provide evidence for the existence of orbits in the unstable manifold of certain periodic orbits that connect to toroidal objects in phase space. These connections exist for specific initial points in the fundamental domain, i.e., along the line $\mathbf{u}(0) + \varepsilon\mathbf{v}(0)$, $\varepsilon \in [\varepsilon_1, \varepsilon_2]$. The connecting orbits are generated numerically as the initial value of the orbits approaches a final point inside the fundamental domain, as the integration time T_r increases and additional windings are generated near the end of the orbit. As a consequence the fundamental domain is not fully covered, although this can be remedied by repeating the entire sequence of steps in the algorithm, starting from a value of ε that corresponds to a point in the part of the fundamental domain that is not covered.

The question arises as to what happens to the periodic-orbit-to-torus connections if the periodic orbit is varied along one of the primary or secondary families. One approach would be to repeat the computations for each one of a sequence of periodic orbits along a given family, e.g., along the halo family H_1. However, here also, continuation is a more effective tool that allows interesting connecting orbits to be detected easily along the continuation path.

We are then led to consider the following approach: collect the equations that define the periodic orbit (Eqs. (2), (4), (5)), the equations defining the Floquet multiplier and eigenfunction (Eq. (7)), and the equations for the orbit in the unstable manifold (Eq. (11)). For clarity, this complete set of coupled equations is reproduced in Eq. (13).

$$
\begin{aligned}
\dot{\mathbf{u}}(t) &= T\,\mathbf{f}(\mathbf{u}(t), \sigma), \\
\mathbf{u}(1) &= \mathbf{u}(0), \\
\int_0^1 \langle \mathbf{u}(t), \dot{\mathbf{u}}_0(t)\rangle dt &= 0, \\
\dot{\mathbf{v}}(t) &= T\mathbf{f_u}(\mathbf{u}(t), 0)\mathbf{v}(t) + \lambda\mathbf{v}(t), \\
\mathbf{v}(1) &= \mathbf{v}(0), \\
\langle \mathbf{v}(0), \mathbf{v}(0)\rangle &= \rho, \\
\dot{\mathbf{r}}(t) &= T_r\,\mathbf{f}(\mathbf{r}(t), 0), \\
\mathbf{r}(0) &= \mathbf{u}(0) + \varepsilon\mathbf{v}(0), \\
\mathbf{r}(1)_x &= x_\Sigma, \\
\int_0^1 \langle \mathbf{w}(t) - \mathbf{w}_0(t), \mathbf{w}_0'(t)\rangle dt + \langle \mathbf{p} - \mathbf{p}_0, \mathbf{p}_0'\rangle &= \Delta s, \\
\mathbf{w}(t) = (\mathbf{u}(t), \mathbf{v}(t), \mathbf{r}(t)), \quad \mathbf{p} &= (T, \sigma, \lambda, \varepsilon)
\end{aligned}
\tag{13}
$$

The last constraint shown in Eq. (13) is the suitably expanded version of the pseudo-arc-length constraint (Eq. (6)) that defines the continuation step size.

Recall that each of the vectors $\mathbf{u}$, $\mathbf{v}$, and $\mathbf{r}$, is six-dimensional. A simple count shows that Eq. (13) represents a system of 18 ODEs, subject to a total of 21 boundary and integral constraints, not counting the pseudo-arclength constraint. Generically, the continuation of a solution to Eq. (13) then requires four free scalar variables. The appropriate choice of these parameters is T, σ, λ, and ε, where T is the period of $\mathbf{u}(t)$, σ is the unfolding parameter, e^λ is the Floquet multiplier, and ε corresponds to the step size in the direction of the unstable manifold.

The BVP in Eq. (13) does not directly define a connection from a periodic orbit to a torus, but a connection from a periodic orbit to a section Σ for a sufficiently large, fixed, value of the integration time T_r of $\mathbf{r}(t)$. The torus is then indirectly continued. This indirect approach is very useful as the direct approach is known to be of considerable algorithmic complexity, as addressed for example in Dieci et al. (1991), Dieci and Lorenz (1995), Edoh et al. (1995), Henderson (2002), Schilder et al. (2005), Olikara (2010).

The strategy of indirect continuation is somewhat analogous to the computation of a simple homoclinic orbit, i.e., an orbit in phase space that approaches a given saddle equilibrium in both positive and negative time. The continuation of such a homoclinic orbit in two parameters can be directly formulated as a boundary value problem with asymptotic boundary conditions that compute the saddle point and its relevant eigenspaces. In fact, this approach has been used very effectively for the continuation of homoclinic and heteroclinic orbits, including higher co-dimension orbits, both for orbits homoclinic or heteroclinic to equilibria or to periodic orbits (Champneys et al. 1996). However, a generic homoclinic orbit can also be very effectively approximated indirectly by a periodic orbit of high period, which renders the 2-parameter continuation of a homoclinic orbit as simple as the continuation of a periodic orbit (using the techniques given in Sect. 3) where the period T is fixed at a sufficiently large value.

In the next section we demonstrate the use of the indirect periodic-orbit-to-torus approach described above, by applying it to the connecting orbits from a halo orbit in the H_1 family to a torus, as initially computed in Sect. 5. We will see that these continuation calculations can lead to approximate connecting orbits from the base periodic orbit to resonant periodic orbits and to other periodic orbits. The detection of such approximate connections can be refined, which we do not do in this paper, to provide more accurate approximations to such connecting orbits. These, in turn, can then be continued directly, using known algorithms for this purpose, as described, for example, in Champneys et al. (1996), Doedel et al. (2008, 2009), and as implemented in AUTO.

7 Showcasing three families of connecting orbits

In this section we describe the results of the further continuation of orbits that connect a periodic orbit to a torus, as initially found in Sect. 5. This is done using the 18-dimensional system in Eq. (13), which was discussed in the preceding section.

As a first example we start from the orbit shown in Fig. 13 which connects the H_1 halo orbit with period $T = 2.5152$ and energy $E = -1.5164$ to a quasi-halo toroidal orbit near the originating halo orbit, after making one loop around the Earth. The continuation procedure using the 18-dimensional ODE in Eq. (13) allows the energy to change, and with it the H_1 orbit itself, the connecting orbit, and the torus it approaches. Interesting transitions are encountered along the continuation path, namely, in the way the changing connecting orbit winds around the changing torus.
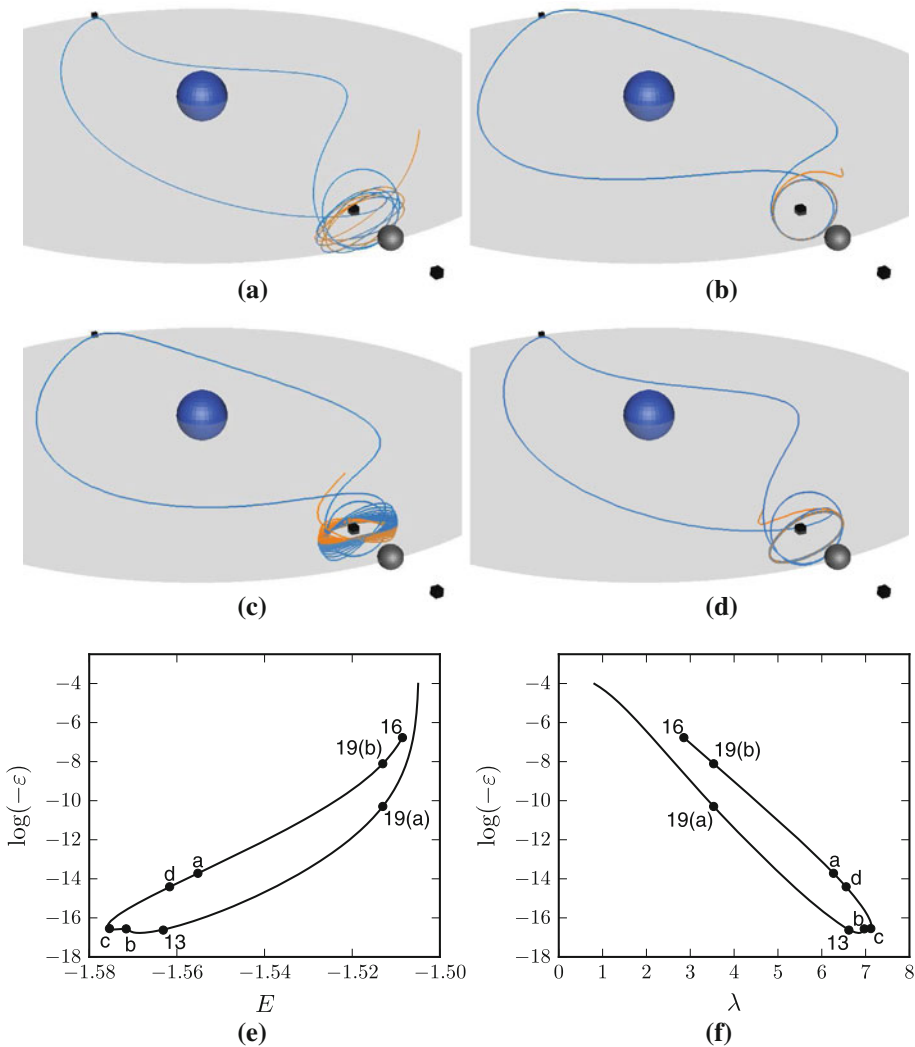
Fig. 15 A family of connecting orbits from H_1 halo orbits to tori, making one loop around the Earth. The terminating plane Σ is located at $x_\Sigma = 0.6$. **a–d** Connecting orbits from H_1 halo orbits to **a** a 5:1 resonant orbit near the corresponding southern halo orbit, **b** approximately the originating H_1 halo orbit, **c** an L_1 planar orbit, and **d** a southern H_1 orbit. **e** Energy of the halo orbit versus $\log(-\varepsilon)$ along the continuation path. The continuation terminates in the top right corner when the Floquet multipliers of the H_1 orbit become complex, and at label 16 in the heteroclinic connection shown in Fig. 16. Labels a–d, 13, 16, and 19a, b correspond to the values in the panels above and in Figs. 13, 16, and 19. **f** The logarithm of the unstable Floquet multiplier of the halo orbit versus $\log(-\varepsilon)$ along the continuation path

Examples are shown in Fig. 15. Panel (a) shows the connecting orbit evidently approaching a 5:1 resonant orbit. In panel (b) the quasi-halo orbit has shrunk so it can not be visually distinguished from the periodic halo orbit in whose unstable manifold it lies, that is, the orbit appears to be homoclinic to the H_1 orbit. Such an orbit could be interesting in space mission design, allowing for occasional large spatial excursions from an H_1 orbit for negligible energy cost. Panel (c) shows a heteroclinic connection between an H_1 orbit and the planar L_1 orbit with the same energy $E = -1.5754$. Recall that the L_1 family is the Lyapunov family that

bifurcates from the libration point $\mathcal{L}_1$, as seen in Fig. 2. This heteroclinic connection could be used for a low cost transfer orbit between the H_1 and L_1 orbits with energy $E = -1.5754$, even though these orbits are different in their dynamical properties (see Figs. 3, 4) and far apart in the bifurcation diagram of the orbits (see Fig. 2). Panel (d) is similar to panel (b), but now the northern halo orbit is connected to its corresponding southern halo orbit, which is the mirror image with respect to the $Z = 0$ plane of the northern halo orbit. That is, the connection appears heteroclinic instead of homoclinic. The energies of these connecting orbits and the periods of the periodic orbits that they connect to, for these and other connecting orbits in this paper, are given in Table 1.

During the same continuation one encounters the connecting orbit seen in Fig. 16. There is still ample evidence of an underlying torus as this figure shows. However, on this torus the connecting orbit oscillates between a northern axial A_1 orbit and its symmetric southern counterpart, each time spending a significant number of rotations very close to each of these two periodic orbits. This suggests a low cost transfer orbit between an H_1 halo orbit and the northern or southern A_1 axial orbit with the same energy $E = -1.5085$. The connecting orbit

Table 1 Numerically computed values for all figures

Figure	Energy	Type	Period	Non-trivial Floquet exponents
7, 9, 10, 11	−1.5164	V_1	3.7700	$\pm 6.4948, \pm 0.077175 \cdot 2\pi i$
12	−1.5532	H_1	2.7873	$\pm 6.1730, \pm 0.21859 \cdot 2\pi i$
		Quasi-H_2	3.2753	$\pm 5.9348, \pm 0.17737 \cdot 2\pi i$
13	−1.5631	H_1	2.7821	$\pm 6.6179, \pm 0.16367 \cdot 2\pi i$
14	−1.5733	H_1	2.7716	$\pm 7.0356, \pm 0.11217 \cdot 2\pi i$
		Quasi-H_2	3.3805	$\pm 6.7839, \pm 0.068079 \cdot 2\pi i$
15a	−1.5552	Quasi-H_1 (5:1 res)	2.7868	$\pm 6.2673, \pm 0.20690 \cdot 2\pi i$
15b	−1.5716	H_1	2.7736	$\pm 6.9682, \pm 0.12050 \cdot 2\pi i$
15c	−1.5754	H_1	2.7690	$\pm 7.1183, \pm 0.10189 \cdot 2\pi i$
		L_1	2.8982	$\pm 0.29251, \pm 7.4268$
15d	−1.5617	H_1	2.7832	$\pm 6.5556, \pm 0.17135 \cdot 2\pi i$
8, 16	−1.5085	H_1	2.5152	$\pm 2.8541, \pm 0.38928 \cdot 2\pi i$
		A_1	4.0117	$\pm 0.43035, \pm 6.1278$
17a	−1.5276	H_1	2.7472	$\pm 4.7666, \pm 0.39460 \cdot 2\pi i$
		L_2	3.9550	$\pm 5.9229, \pm 0.52353$
17b	−1.5679	H_1	2.7776	$\pm 6.8207, \pm 0.13870 \cdot 2\pi i$
		H_2	3.3567	$\pm 6.5802, \pm 0.095719 \cdot 2\pi i$
17c	−1.5349	H_1	2.7715	$\pm 5.2225, \pm 0.33730 \cdot 2\pi i$
		Quasi-H_2 (5:1 res)	3.1170	$\pm 4.9006, \pm 0.30348 \cdot 2\pi i$
17d	−1.5303	H_1	2.7581	$\pm 4.9440, \pm 0.23394 \cdot 2\pi i$
		Quasi-H_2 (6:1 res)	3.0568	$\pm 4.5639, \pm 0.34345 \cdot 2\pi i$
18a	−1.5728	H_1	2.7722	$\pm 7.0158, \pm 0.11462 \cdot 2\pi i$
		Quasi-H_2	3.3784	$\pm 6.7651, \pm 0.070727 \cdot 2\pi i$
19	−1.5130	H_1	2.6176	$\pm 3.5327, \pm 0.45736 \cdot 2\pi i$

Each line with Figure and Energy values contains the data for the starting periodic orbit $\mathbf{u}(t)$. If the orbit $\mathbf{r}(t)$ connects the periodic orbit to a different periodic orbit, or to a torus that surrounds a different periodic orbit (a quasi-periodic orbit), then the following line row contains data for this second periodic orbit. There are always two trivial Floquet exponents equal to zero

between the northern and southern axial orbits is generic, as will be shown in the next section. Evidence of tori close to heteroclinic connections between two symmetric axial families can also be found in Fig. 1 of Gómez and Mondelo (2001) for an energy value (corresponding to Fig. 19 discussed later) not far from that of Fig. 16. In Gómez and Mondelo (2001) the axial orbits are denoted by diamond-shaped fixed points.

Figure 15e depicts the change of ε versus the energy, where the labels correspond to the values of panels (a)–(d) and Figs. 13, 16, and 19. Note that for most energy values in this range there exist two connections with different values of ε. The continuation terminates at two points on the right hand side of this diagram, because the Newton-chord method that AUTO employs no longer converges there. One of these points corresponds to the special connecting orbit in Fig. 16. For the other termination point the unstable real Floquet multiplier reaches the unit circle, so the two-dimensional unstable manifold ceases to exist. Figure 15f and the thin-to-thick curve transition for H_1 in Fig. 2a show this Floquet multiplier behavior.

The apparent connections from an H_1 halo orbit to an L_2 planar orbit, an H_2 halo orbit, and 5:1 and 6:1 resonant orbits shown in Fig. 17a–d result from the continuation of the connecting orbit in Fig. 12, again using the 18-dimensional system in Eq. (13). In this case the connecting orbit makes four loops (instead of just one as in Fig. 15) around the Earth. Here also, the continuation passes through many resonances. Specifically, the connecting orbits shown in panels (c) and (d) of Fig. 17 approach a period-5 orbit and a period-6 orbit, respectively.

We reiterate that the originating H_1 halo orbit changes during the continuation, and with it its period and energy. Consequently the energy of the connecting orbit as well as the energy of the torus that it approaches change with it, as these energies are identical. Similar to panels (e) and (f) of Fig. 15, Fig. 17 show diagrams for the energy and Floquet exponents. Note however, that in this case the continuation does not terminate but loops around, and for every energy value between the two extrema there exist two connecting orbits. Numerically it was observed that the value of $\log(-\varepsilon)$ is always close to -2λ, so to visualize the loop these two quantities were subtracted in panel (f).

Note that the two extrema in panels (e) and (f) are detected as folds by the continuation software, and that these could in turn be followed, for instance by adding the mass-ratio μ as a free parameter. The folds themselves do not appear to correspond to particularly interesting orbits (panels a and b in Fig. 17 are close to but not at the fold locations).

Similarly, Fig. 18a shows an interesting orbit from the continuation of the connecting orbit in Fig. 14, namely a direct connection, *without* looping around the Earth, from an H_1 orbit to an L_2 Lyapunov orbit. Figure 18b, c show diagrams much like those in Fig. 17, where the continuation curve is a loop. However, compared to Fig. 17, here the range of the energy level and the differences between values of $\log \varepsilon$ are greater. Also note that the sign of ε is always positive, rather than negative as before, as we are now considering the Moon side of the unstable manifold of the H_1 orbits and so the sign of ε in Eq. (13) is changed.

8 Existence of connecting orbits

As seen in the preceding sections, boundary value formulations provide a powerful tool to compute unstable manifolds and connecting orbits in the CR3BP. Our exploration shows only the tip of the iceberg of a wealth of interesting orbits. This section discusses how the connecting orbits that were found relate to the existing literature. As mentioned in Sect. 1, the periodic orbits and tori themselves, as well as homoclinic and heteroclinic orbits connecting
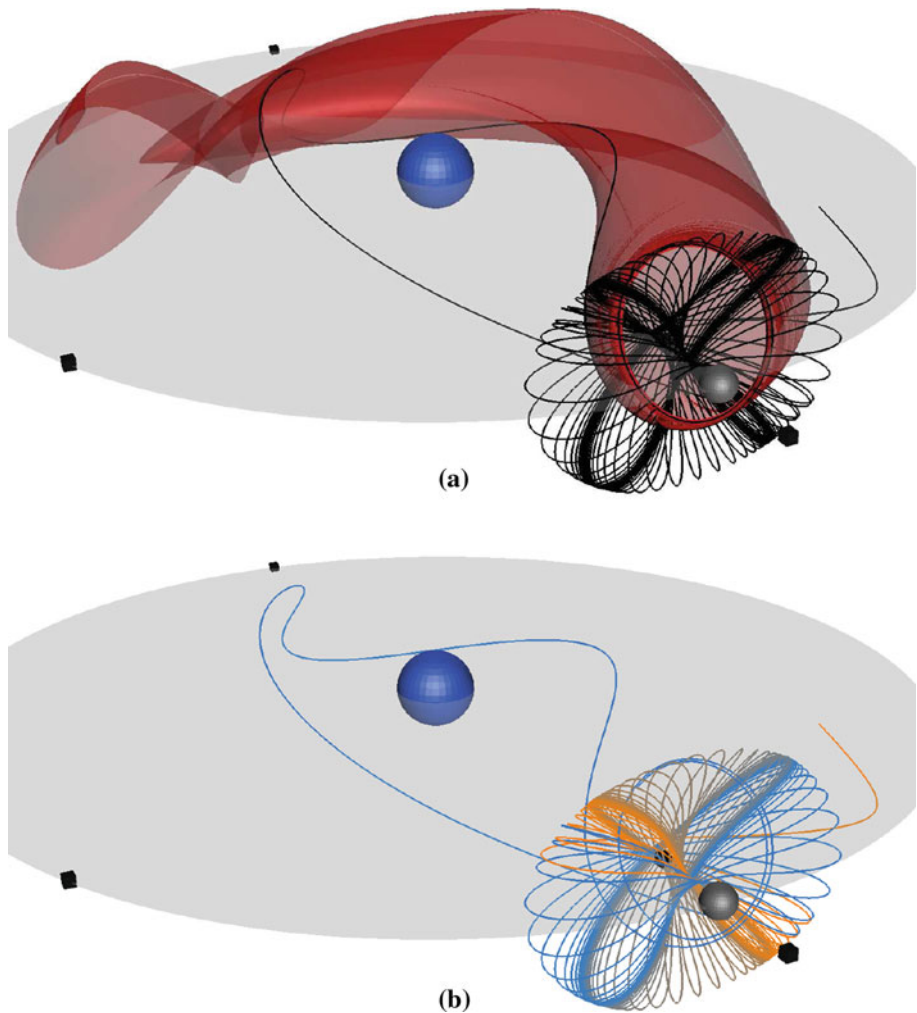
Fig. 16 **a** The unstable manifold of the H_1 periodic orbit from Fig. 8, together with a superimposed longer orbit that was found by continuation using the 18-dimensional system in Eq. (13). **b** A separate view of the orbit in the unstable manifold. This orbit returns near the originating H_1 periodic orbit, where it winds around a quasi-halo orbit, while spending significant time near a northern axial A_1 orbit and its symmetric southern counterpart. As is clearly visible, and as required by the computational formulation, the orbit ultimately returns to the plane Σ, located at $x_\Sigma = 0.6$

L_1 and L_2 periodic orbits have been studied extensively. However, for the spatial case, to the best of our knowledge, connecting orbits from H_1 halo to quasi-H_1 or quasi-H_2 have not been explicitly found before. We must mention that connections from quasi-H_1 to quasi-H_2 orbits can be found in Gómez et al. (2004).

In all three continuations in Sect. 7 a collection of interesting objects was seen, including apparent heteroclinic connections between halo orbits and resonant orbits, i.e., seemingly heteroclinic connections between halo orbits and n-periodic orbits, where the complex Floquet multipliers of the halo orbit near the n-periodic orbit are close to $e^{2\pi i/n}$. Numerical data corresponding to figures in this paper are given to 5 significant digits in Table 1.
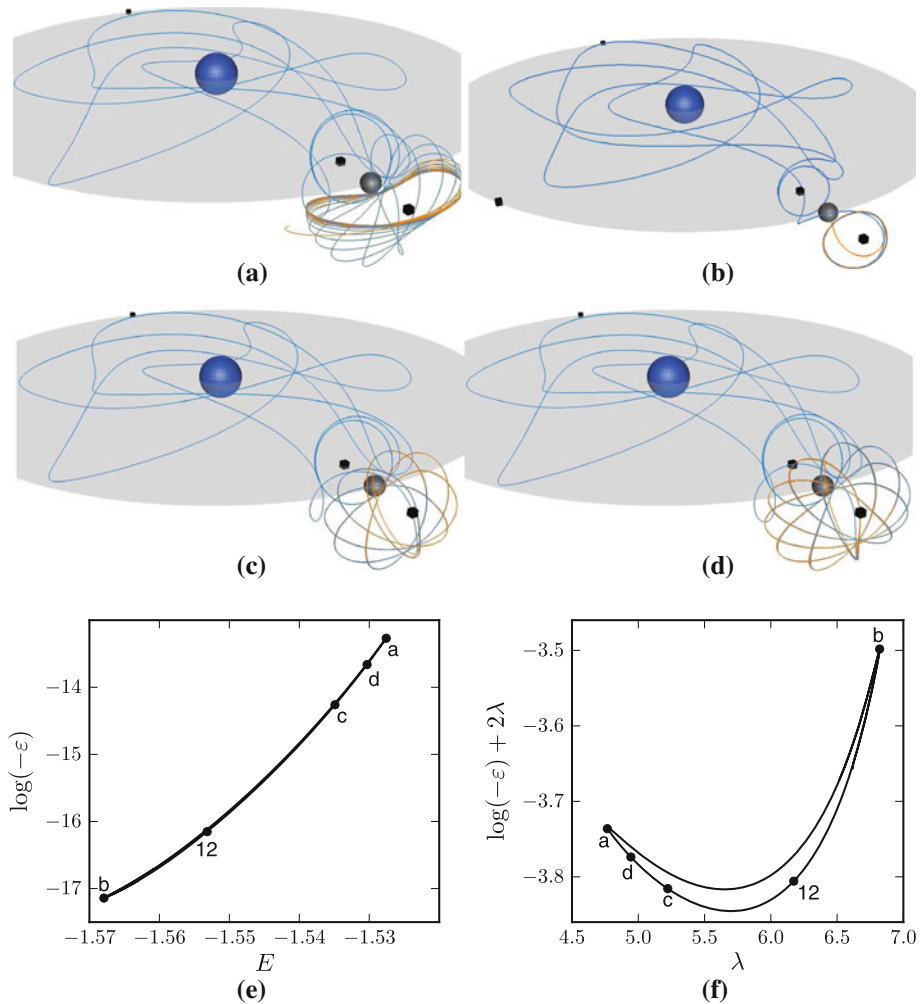
Fig. 17 A family of connecting orbits from H_1 halo orbits to tori, making four loops around the Earth. The terminating plane Σ is located at $x_\Sigma = 1.02$. **a–d** Connecting orbits from H_1 halo orbits to **a** a planar L_2 Lyapunov orbit, **b** approximately an H_2 halo orbit, **c** a 5:1 resonant orbit near the libration point $\mathscr{L}_2$, and **d** a 6:1 resonant orbit. **e** Energy versus $\log(-\varepsilon)$ along the continuation path. The continuation curve is a loop. Labels a–d and 12 correspond to the values in the panels above and in Fig. 12. **f** The logarithm λ of the unstable Floquet multiplier of the halo orbit versus $\log(-\varepsilon) + 2\lambda$ along the continuation path. Here $\log(-\varepsilon) + 2\lambda$ is plotted instead of $\log(-\varepsilon)$ to make the loop visible

The existence of certain connecting orbits can be explained by counting dimensions. For Fig. 16, the multipliers of the symmetric axial orbits give rise to three-dimensional stable and unstable manifolds, so the connection between the two northern and southern A_1 axial orbits seen in Fig. 16 is generic for the CR3BP posed in $\mathbb{R}^6$. The connection from the H_1 halo orbit to the A_1 axial orbit is codimension-one, since the H_1 halo orbit has a two-dimensional unstable manifold, and the stable manifold of the A_1 axial orbit is three-dimensional. Similarly the planar L_1 and L_2 Lyapunov orbits for the energy values that we observe in Figs. 15c, 17a and 18a have three-dimensional stable and unstable manifolds, so connections from H_1 halo Orbits to those orbits are also codimension-one. By standard bifurcation theory,
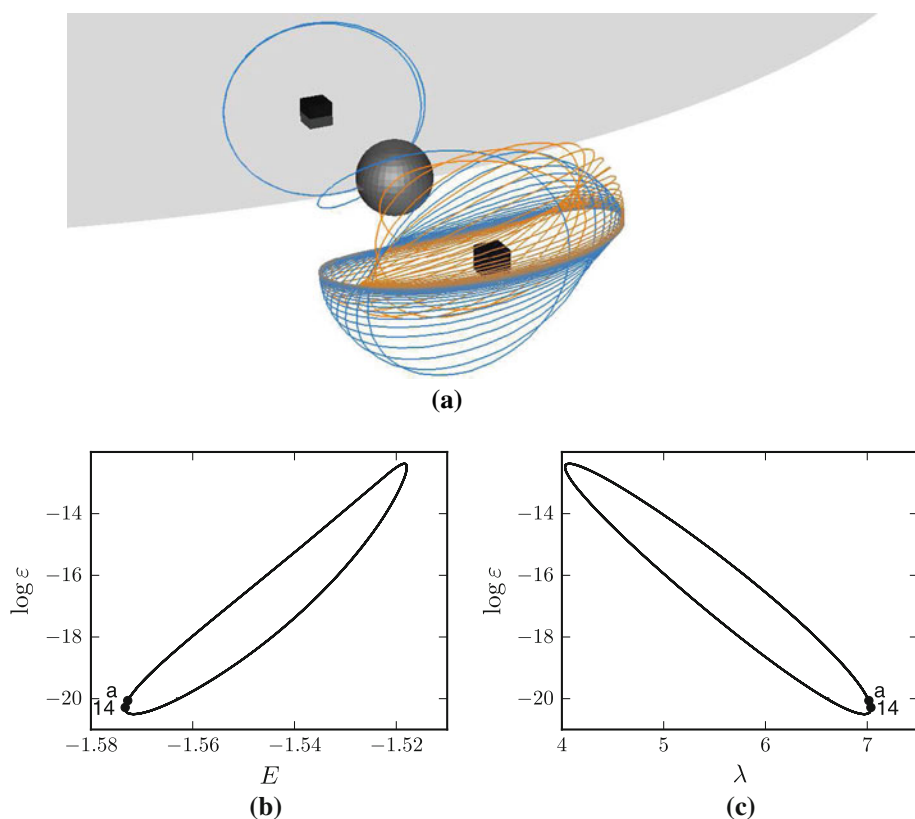
(a)

(b)

(c)

Fig. 18 **a** An orbit directly connecting the Moon side of the unstable manifold of the H_1 orbit with $E = -1.5728$ to an L_2 Lyapunov orbit, obtained by continuation of the orbit shown in Fig. 14. **b** Energy versus $\log(\varepsilon)$ along the continuation path. The continuation curve is a loop. Labels a and 14 correspond to the values in the panels above and in Fig. 14. **c** The logarithm of the unstable Floquet multiplier of the halo orbit versus $\log(\varepsilon)$ along the continuation path

codimension-one connecting orbits can be expected to arise as one parameter is varied, for specific values of that parameter. This is indeed what we observed in these cases, where we found such connecting orbits for specific values of the energy E.

8.1 Connecting orbits from a halo orbit to a quasi-halo orbit

In contrast to the connecting orbits considered above, the connections from the H_1 halo orbit to the same or other halo orbits cannot simply be explained by counting dimensions. The H_1 halo orbit has a two-dimensional unstable manifold and a two-dimensional stable manifold, so such connections would be codimension-two and would not be expected along a family (in the sense of this paper) of halo orbits. The apparent halo orbits in the halo to halo connecting orbits may in fact be very thin quasi-halo orbits (tori). However, even if this distinction were mathematically important, it would presumably be of little practical importance in space mission design.

We justify the presence of the connecting orbits from H_1 halo orbits to quasi-halo orbits by recalling the detailed analysis of center manifolds around collinear libration points in Jorba
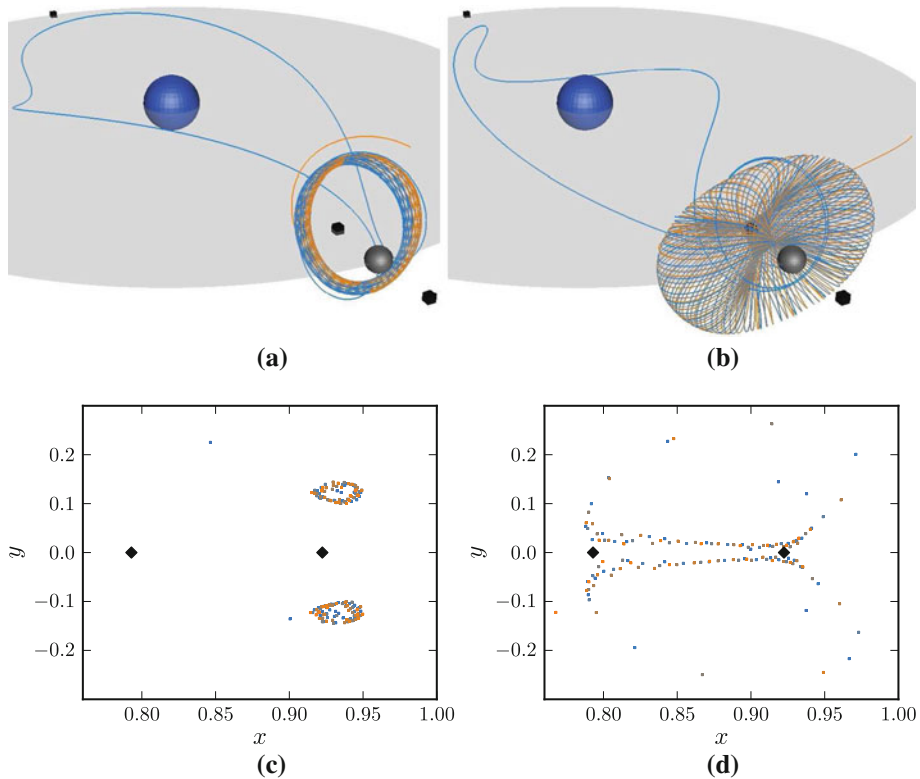
Fig. 19 **a** and **b** Two orbits for the family displayed in Fig. 15 where $E = -1.5130$. **c** and **d** Their intersections with the plane $z = 0$. The energy value corresponds to Fig. 1 in Gómez and Mondelo (2001) and Fig. 3 in Alessi et al. (2009), where the energy is denoted as $h = E + \mu(1 - \mu)/2 = -1.507$. The two diamonds correspond to intersections of the A_1 axial orbits, as in Gómez and Mondelo (2001)

and Masdemont (1999), Gómez et al. (2004), and Koon et al. (2008). For a prescribed energy level, the thin solid curves in Fig. 2 show that there exists a halo orbit near $\mathscr{L}_i$, for $i = 1, 2$, that has two complex Floquet multipliers on the unit circle and different from one. There are two more real Floquet multipliers, one of them greater than one and the other less than one. The Floquet multipliers and corresponding energy levels for the halo orbits in Figs. 8 and 12 to 19 are shown in Table 1.

The unstable manifold of such a halo orbit is a two-dimensional surface, see Fig. 8. On the other hand, close to either of the two libration points $\mathscr{L}_j$, for $j = 1, 2$, there is a four-dimensional center manifold, which exists due to the fact that $\mathscr{L}_j$ has four eigenvalues on the unit circle and two more on the real line excluding one.

On the energy surface the center manifold of the co-linear libration points is a little different. In Koon et al. (2008) the authors verify that for fixed energy, the center manifold of $\mathscr{L}_j$, for $j = 1, 2$, is a normally hyperbolic invariant manifold (NHIM) corresponding to a normally hyperbolic three-sphere that is invariant for the linearized system. Thus, in a small neighborhood of $\mathscr{L}_j$ the center manifold becomes a deformed three-sphere for the nonlinear system. Moreover, it is a three-dimensional hyperbolic invariant manifold in a five-dimensional energy surface with one stable direction. Therefore the stable manifold of the center manifold is four-dimensional.

In this setting, dimension counting gives a heuristic argument that motivates why connecting orbits from halo orbits to torus-like objects appear quite naturally in our problem, as seen in Figs. 12, 13, 14 and 19. We have mentioned that the center manifold of a libration point $\mathscr{L}_i$ restricted to the energy surface is a three-dimensional NHIM, so we can do dimension counting analyses similar to those above. The main observation is that for a fixed value of the energy, these quasi-halo orbits are lower dimensional whiskered quasi-periodic solutions (see Fontich et al. 2009) that lie inside the three-dimensional center manifolds of the collinear libration points.

Now, the halo orbit is a one-dimensional normally hyperbolic object with one unstable direction. The halo orbit itself also belongs to the center manifold of $\mathscr{L}_i$ and its unstable manifold is a two-dimensional object in the energy surface. Finally, by dimension counting, we notice that a transversal intersection between the unstable manifold of the halo orbit of $\mathscr{L}_j$ and the stable manifold of the center manifold of $\mathscr{L}_j$ is a one-dimensional object.

Several authors (Jorba and Masdemont 1999; Masdemont 2005; Alessi et al. 2009) have explored the center manifolds of collinear libration points by means of Lindstedt-Poincaré expansions of the Hamiltonian restricted to each center manifold. These computations suggest that for the energy levels under consideration in this paper there exist large regions in the center manifold that exhibit quasi-periodic motions. The $z = 0$ sections of the center manifolds reveal that most of these quasi-periodic obits are two-dimensional invariant tori in the center manifold (see for instance Fig. 3 in Alessi et al. (2009)). These invariant tori are also normally hyperbolic and their corresponding stable manifolds are two-dimensional objects inside the four-dimensional stable manifold of the center manifold. These codimension-one stable manifolds separate the four-dimensional stable manifold into regions.

A trajectory in the intersection of the unstable manifold of the halo orbit and the stable manifold of the center manifold has a positive probability of being either on the stable manifold of an invariant torus or in a region bounded by stable manifolds of invariant tori. It is even possible that the trajectory belongs to the stable manifold of a periodic orbit (e.g., a halo orbit) in the center manifold of $\mathscr{L}_j$. However, this is unlikely since the stable manifold of a periodic orbit is a two-dimensional object inside a four-dimensional stable manifold. Thus, it is more likely that a trajectory in the intersection of the unstable manifold of a halo orbit with the stable manifold of the three-dimensional center manifold of a libration point passes close to a two-dimensional hyperbolic quasi-periodic orbit in the center manifold.

Figure 19a, b show two connections from a halo orbit to a quasi-halo orbit nearby, from the continuation displayed in Fig. 15, where the energy value $E = -1.5130$ matches the value $h = -1.507$ used for Fig. 1 in Gómez and Mondelo (2001) and Fig. 3 in Alessi et al. (2009), where $h = E + \mu(1+\mu)/2$. In Fig. 19c, d we show the intersections of these trajectories with the plane $z = 0$. If we compare these intersections to the corresponding ones in Gómez and Mondelo (2001) and Alessi et al. (2009), we discover that the trajectory seems to approach one of these quasi-halo orbits and then drift away from it. We conclude that the trajectory computed by our methods is shadowing a connecting orbit in the intersection of the unstable manifold of the halo orbit and the stable manifold of the corresponding normally hyperbolic lower dimensional torus.

9 Numerical aspects

In our computations we used the continuation and bifurcation software AUTO (Doedel 1981; Doedel et al. 2010) for computing families of periodic orbits, associated Floquet eigenfunctions, unstable manifolds, and connecting orbits. Orbits are continued in AUTO as solutions to

a suitable boundary value problem (BVP), as described in this paper. To compute approximate solutions of BVPs, AUTO uses the method of Gauss–Legendre collocation with piecewise polynomials on adaptive meshes (de Boor and Swartz 1973; Ascher et al. 1981). These calculations can be fast; for example the *entire* vertical family of periodic orbits V_1 can be computed in 0.12 s on a dual core laptop, using as few as 20 mesh intervals with 4 Gauss collocation points each, and using 48 continuation steps. In our actual computations we use more mesh intervals to ensure high accuracy, e.g., with 100 mesh intervals the family V_1 can be computed in 0.25 s. We also often use more continuation steps, for example for the purpose of generating data for computer animations.

Two-dimensional unstable manifolds computed as a solution family by continuation, as done in Sect. 4, require more mesh intervals and continuation steps when the orbits in the family wind many times around a torus. For example, a connection from the halo orbit H_1 to a torus near H_2, winding around the torus 12 times, can be reached easily in 15 s, using 200 mesh intervals and 1,000 continuation steps. However, we also computed such connections with a much higher number of windings, which requires a correspondingly higher number of mesh intervals and continuation steps. In fact, we have used up to 1,500 mesh intervals in such cases. Furthermore, to ascertain the correctness of our results, we have computed these manifolds with various choices of the number of mesh intervals.

Similarly, the continuation of solutions to the 18-dimensional system to follow periodic-orbit-to-torus connections, as given in Sect. 6 and used in Sect. 7, requires a correspondingly high number of mesh intervals. Since the dimension of the system is then 18, i.e., three times the dimension of the systems used for continuing periodic orbits and unstable manifolds, the computation time would increase by a factor 3^3, that is 27. However, this is reduced since AUTO takes into account the zero structure of the submatrices of the full Jacobian matrix that correspond to individual mesh intervals. On the other hand, the connecting orbit requires significantly more mesh intervals than the base periodic orbit and its Floquet eigenfunction, and AUTO does not take advantage of this. Thus the continuation of the coupled system (periodic orbit, Floquet eigenfunction, connecting orbit) in Sect. 6 can take significant computer time, also because such continuation with varying energy requires many continuation steps. In extreme cases the calculations have taken up to 6 h computer time.

References

Aguirre, P., Doedel, E.J., Krauskopf, B., Osinga, H.M.: Investigating the consequences of global bifurcations for two-dimensional invariant manifolds of vector fields. Discret. Contin. Dyn. Syst. **29**, 1309–1344 (2011)

Alessi, E.M., Gómez, G., Masdemont, J.: Leaving the Moon by means of invariant manifolds of libration point orbits. Commun. Nonlinear Sci. Numer. Simul. **14**, 4153–4167 (2009)

Ascher, U.M., Christiansen, J., Russell, R.D.: Collocation software for boundary value ODEs. ACM Trans. Math. Softw. **7**, 209–222 (1981)

Barrabés, E., Mondelo, J.M., Ollé, M.: Numerical continuation of families of homoclinic connections of periodic orbits in the RTBP. Nonlinearity **22**, 2901–2918 (2009)

Canalias, E., Masdemont, J.J.: Homoclinic and heteroclinic transfer trajectories between planar Lyapunov orbits in the Sun–Earth and Earth–Moon systems. Discret. Contin. Dyn. Syst. **14**, 261–279 (2006)

Champneys, A.R., Kuznetsov, Yu.A., Sandstede, B.: A numerical toolbox for homoclinic bifurcation analysis. Int. J. Bifurcation Chaos Appl. Sci. Eng. **6**, 867–887 (1996)

Danby, J.M.A.: Fundamentals of Celestial Mechanics. Willmann-Bell, Richmond, VA (1992)

Davis, K.E., Anderson, R.L., Scheeres, D.J., Born, G.H.: The use of invariant manifolds for transfers between unstable periodic orbits of different energies. Celest. Mech. Dyn. Astron. **107**, 471–485 (2010)

Davis, K.E., Anderson, R.L., Scheeres, D.J., Born, G.H.: Optimal transfers between unstable periodic orbits using invariant manifolds. Celest. Mech. Dyn. Astron. **109**, 241–264 (2011)

de Boor, C., Swartz, B.: Collocation at Gaussian points. SIAM J. Numer. Anal. **10**, 582–606 (1973)

Delshams, A., Masdemont, J., Roldán, P.: Computing the scattering map in the spatial Hill's problem. Discret. Contin. Dyn. Syst. Ser. B **10**, 455–483 (2008)

Dieci, L., Lorenz, J.: Computation of invariant tori by the method of characteristics. SIAM J. Num. Anal. **32**, 1436–1474 (1995)

Dieci, L., Lorenz, J., Russell, R.D.: Numerical calculation of invariant tori. SIAM J. Sci. Stat. Comput. **12**, 607–647 (1991)

Doedel, E.J.: AUTO: a program for the automatic bifurcation analysis of autonomous systems. Cong. Num. **30**, 265–284 (1981)

Doedel, E.J., Paffenroth, R.C., Keller, H.B., Dichmann, D.J., Galán-Vioque, J., Vanderbauwhede, A.: Continuation of periodic solutions in conservative systems with applications to the 3-body problem. Int. J. Bifurcation Chaos Appl. Sci. Eng. **13**, 1–29 (2003)

Doedel, E.J., Krauskopf, B., Osinga, H.M.: Global bifurcations of the Lorenz manifold. Nonlinearity **19**, 2947–2972 (2006)

Doedel, E.J., Romanov, V.A., Paffenroth, R.C., Keller, H.B., Dichmann, D.J., Galán-Vioque, J., Vanderbauwhede, A.: Elemental periodic orbits associated with the libration points in the circular restricted 3-body problem. Int. J. Bifurcation Chaos Appl. Sci. Eng. **17**, 2625–2677 (2007)

Doedel, E.J., Kooi, B.W., Van Voorn, G.A.K., Kuznetsov, Yu.A.: Continuation of connecting orbits in 3D-ODEs (II): point-to-cycle connections. Int. J. Bifurcation Chaos Appl. Sci. Eng. **18**, 1889–1903 (2008)

Doedel, E.J., Kooi, B.W., Van Voorn, G.A.K., Kuznetsov, Yu.A.: Continuation of connecting orbits in 3D-ODEs (II): cycle-to-cycle connections. Int. J. Bifurcation Chaos Appl. Sci. Eng. **19**, 159–169 (2009)

Doedel, E.J., Oldeman, B.E., et al.: AUTO-07P: Continuation and Bifurcation Software for Ordinary Differential Equations. Concordia University, Montréal (2010). http://cmvl.cs.concordia.ca/auto/

Doedel, E.J., Krauskopf, B., Osinga H.M.: Global invariant manifolds in the transition to preturbulence in the Lorenz system, Indagationes Mathematicae **22**, 222–240 (2011)

Dunham, D.W., Farquhar, R.W.: Libration point missions. In: Gómez, G., Lo, M.W., Masdemont, J.J. (eds.) Libration Point Orbits and Applications, 1978–2002, pp. 45–73. World Scientific, Singapore (2003)

Edoh, K.D., Russell, R.D., Sun, W.: Orthogonal Collocation for Hyperbolic PDEs & Computation of Invariant Tori, Australian National Univ., Mathematics Research Report No. MRR 060-95 (1995)

Fairgrieve, T.F., Jepson, A.D.: O.K. Floquet multipliers. SIAM J. Numer. Anal. **28**, 1446–1462 (1991)

Farquhar, R.W.: The Control and Use of Libration-Point Satellites, Ph.D. Dissertation, Dept. of Aeronautics and Astronautics, Stanford University, Stanford (1968)

Fontich, E., de la Llave, R., Sire, Y.: Construction of invariant whiskered tori by a parameterization method. I. Maps and flows in finite dimensions. J. Differ. Equ. **8**, 3136–3213 (2009)

Gómez, G., Mondelo, J.M.: The dynamics around the collinear equilibrium points of the RTBP. Phys. D **157**, 283–321 (2001)

Gómez, G., Jorba, À., Simó, C., Masdemont, J.: Dynamics and mission design near libration points. Vol. III. World Scientific Monograph Series in Mathematics **4** ISBN 981-02-4211-5 (2001)

Gómez, G., Koon, W.S., Lo, M.W., Marsden, J.E., Masdemont, J., Ross, S.D.: Connecting orbits and invariant manifolds in the spatial restricted three-body problem. Nonlinearity **17**, 1571–1606 (2004)

Goudas, C.L.: Three-dimensional periodic orbits and their stability. Bull. Soc. Math. Grèce, Nouvelle série **2**, 1–22 (1961)

Henderson, M.E.: Multiple parameter continuation: computing implicitly defined k-manifolds. Int. J. Bifurcation Chaos Appl. Sci. Eng. **12**, 451–476 (2002)

Hénon, M.: Vertical stability of periodic orbits in the restricted problem. I. Equal masses. Astron. Astrophys. **28**, 415–426 (1973)

Jorba, À., Masdemont, J.: Dynamics in the center manifold of the collinear points of the restricted three body problem. Phys. D. **132**, 189–213 (1999)

Keller, H.B.: Numerical solution of bifurcation and nonlinear eigenvalue problems. In: Rabinowitz, P.H. (ed.) Applications of Bifurcation Theory, pp. 359–384. Academic Press, New York (1977)

Koon, W.S., Lo, M.W., Marsden, J.E., Ross, S.: Dynamical Systems, the Three-Body Problem and Space Mission Design. Marsden Books (2008). ISBN 978-0-615-24095-4. http://www.cds.caltech.edu/~marsden/volume/missiondesign/KoLoMaRo_DMissionBk.pdf

Krauskopf, B., Osinga, H.M.: Computing invariant manifolds via the continuation of orbit segments. In: Krauskopf, B., Osinga, H.M., Galán-Vioque, J.M. (eds.) Numerical Continuation Methods for Dynamical Systems, pp. 117–154. Springer, New York (2007)

Krauskopf, B., Osinga, H.M., Galán-Vioque, J.M.: Numerical Continuation Methods for Dynamical Systems. Springer, New York (2007)

Krauskopf, B., Rieß, T.: A Lin's method approach finding and continuing heteroclinic connections involving periodic orbits. Nonlinearity **21**, 1655–1690 (2008)

Llibre, J., Martínez, R., Simó, C.: Tranversality of the invariant manifolds associated to the Lyapunov family of periodic orbits near L_2 in the restricted three-body problem. J. Differ. Equ. **58**, 104–156 (1985)

Lo, M.W., Ross, S.D.: Surfing the solar system: invariant manifolds and the dynamics of the solar system. JPL IOM **312**, 2–4 (1997)

Lo, M., Williams, B., Bollman, W., Han, D., Hahn, Y., Bell, J., Hirst, E.: Genesis mission design. J. Astronaut. Sci. **41**, 169–184 (2001)

Lo, M.W., Anderson, R., Whiffen, G., Romans, L.: The role of invariant manifolds in low thrust trajectory design JPL. Nat. Aeronaut. Space Admin. **119**, 2971–2990 (2004)

Masdemont, J.J.: High-order expansions of invariant manifolds of libration point orbits with applications to mission design. Dyn. Syst. **20**, 59–113 (2005)

Muñoz-Almaraz, F.J., Freire-Macias, E., Galán-Vioque, J., Doedel, E.J., Vanderbauwhede, A.: Continuation of periodic orbits in conservative and Hamiltonian systems. Phys. D **181**, 1–38 (2003)

Muñoz-Almaraz, F.J., Freire, E., Galán-Vioque, J., Vanderbauwhede, A.: Continuation of normal doubly symmetric orbits in conservative reversible systems. Celest. Mech. Dyn. Astron **97**, 17–47 (2007)

Olikara, Z.P.: Computation of Quasi-Periodic Tori in the Circular Restricted Three-Body Problem. M.Sc. Dissertation, School of Aeronautics and Astronautics, Purdue University, West Lafayette (2010). http://engineering.purdue.edu/people/kathleen.howell.1/Publications/Masters/2010_Olikara.pdf

Schilder, F., Osinga, H.M., Vogt, W.: Continuation of quasi-periodic invariant tori. SIAM J. Appl. Dyn. Syst. **4**, 459–488 (2005)

Szebehely, V.: Theory of Orbits: The Restricted Problem of Three Bodies. Academic Press, New York (1967)

Tantardini, M., Fantino, E., Ren, Y., Pergola, P., Gómez, G., Masdemont, J.J.: Spacecraft trajectories to the L_3 point of the Sun–Earth three-body problem. Celest. Mech. Dyn. Astron **108**, 215–232 (2010)

Wilczak, D., Zgliczyński, P.: Heteroclinic connections between periodic orbits in planar restricted circular three-body problem—a computer assisted proof. Comm. Math. Phys. **234**, 37–75 (2003)

Wilczak, D., Zgliczyński, P.: Heteroclinic connections between periodic orbits in planar restricted circular three body problem II. Comm. Math. Phys. **259**, 561–576 (2005)